

Final Technical Report
on

**Self-Activated Micro Direct-Methanol Fuel Cell
(μ DMFC) at Near Room Temperature**

Micro Power Generation
Contract/Grant Number: DAAH01-1-R001

Program Director:
Dr. Clark T.-C. Nguyen
DARPA/MTO
3701 N. Fairfax Drive,
Arlington, VA 22203-1714

DISTRIBUTION STATEMENT A
Approved for Public Release
Distribution Unlimited

By:
Professor Xiaolin Zhong (PI)
Professor Chih-Ming Ho (co-PI)
Professor Chang-Jin "CJ" Kim (co-PI)
Professor Xiang Zhang (co-PI)
Mechanical and Aerospace Engineering Department
University of California, Los Angeles, CA 90095
and
Professor Chao-Yang Wang (co-PI)
Director, Electrochemical Engine Center
The Pennsylvania State University, University Park, PA 16802

June 15, 2005

20050718 021

Table of Contents

Summary	3
Program Goals	4
Accomplishments	4
Conclusions	49
Publications	50

Summary

This research project was focused on the development and testing of Micro Direct-Methanol Fuel Cells (μ DMFC). A Si-based μ DMFC was developed and its electrochemical characteristics studied. The peak power density reached 50 mW/cm^2 at 60°C . A new MEA design was successfully developed to mitigate MeOH crossover without requiring novel membranes. A μ DMFC was also fabricated by using photochemically etched stainless steel bipolar plates and the performance was improved to achieve a maximum power density of 100 mW/cm^2 at 60°C and atmospheric pressure. Water crossover through the membrane was found to be a critical issue to limit direct use of high concentration fuel. A solution using the capillary pressure to push water back from the cathode to anode and a thin membrane such as Nafion 112 has been successfully developed. The net water crossover through the membrane was reduced by a factor of five. This paves the way to directly use concentrated fuel on the anode. An 8-cell air-breathing DMFC stack was developed and demonstrated. Cathode flooding was totally avoided using our newly developed water management strategy. It was found that O_2 transport in air-breathing operation is sufficient. Results also demonstrated that it is feasible to finally use pure methanol in a completely passive DMFC. Experimental results proved the degassing ability of sandwiched membrane breather to separate CO_2 from aqueous methanol fuel stream in the μ DMFC, and we determined that the bubble breathing feature can take a more active role in the microfluidic management of the whole system. Since the bubble breathing rate can be much faster than condensing rate of vapor bubble, which led to inefficiency of most reported micro bubble pumps, our degassing technique with hydrophobic porous membrane opened a great opportunity for a self-pumping mechanism to circulate the fuel inside μ DMFC. A proof-of-concept device was constructed and tested, with electrolysis gas bubbles as the mimic of intrinsically generated gas bubbles in fuel cell. Liquid circulation was demonstrated by tracing fluorescence particles in different part of pump-loop. The precise control of multiphase flows at the microscale is crucial to micro-DMFC development. Through micro channel experiments we showed that wettability (hydrophilic/hydrophobic) as well as the presence of impurities in the fuel dramatically can influence the operating conditions of the device. We developed empirical correlations for the effective viscosity of a mixture of gas and either pure liquid or either liquid with impurities. The effective viscosity allows for the prediction of the energy requirement to drive the fuel in the fuel cells. A numerical simulation tool for flows in microchannels was developed, and validated through micro channel flow studies.

Program Goals

The goal of the project was to develop and demonstrate a novel micro direct-methanol fuel cell as a practical MEMS power source. The micro fuel cell has the following innovative features: high energy efficiency and high power density; fabrication by micromachining technology of MEMS; innovative micro fluidic management on fuel and air flow, and exhaust gas separation. Another feature is scalable packaging by modular micro fuel cell design. The research project consisted of the following six major tasks:

- 1. Design a new micro direct methanol fuel cell based on an innovative fluid management idea to deliver fuel by buoyancy/capillary forces and to separate the exhaust gas by a unique distributed gas breather for micro fuel cells;**
- 2. Develop a CFD simulation design tool, with the capability to simulate bubble transport in microchannels and the gas breathing process to assist the new μ DMFC to meet performance specifications;**
- 3. Development of an advanced membrane-electrode assembly for the μ DMFC to substantially reduce methanol crossover;**
- 4. Fabricate, package, and integrate the μ DMFC by MEMS technology;**
- 5. Conduct extensive experimental testing on the new micro fuel cells for performance quantification and optimization.**
- 6. Integrate the CO₂ breathing feature and self-pumping mechanism into the micro fuel cell.**

Accomplishments

Summary of Accomplishments

In this MPG project, we have carried out research on the development and testing of the micro direct methanol fuel cells. Specifically, we have completed the following tasks:

- 1. An advanced MEA design was successfully developed to mitigate MeOH crossover without requiring novel membranes. A 1.625cm² Si-based micro fuel cell has been fabricated and its electrochemical characterized has been extensively investigated. Further development of the micro DMFCs using photochemically etched stainless steel plates as bipolar plates was carried out. Maximum power density reached 62.5mW/cm² at 40°C and 100mW/cm² at 60°C using ambient air.**
- 2. Flow characteristics in the micro DMFCs have been investigated using a transparent fuel cell. An 8-cell air-breathing DMFC stack was carefully designed. Transport phenomena in this DMFC stack has been extensively investigated.**

3. Demonstrated a fully passive DMFC cell. There is no moving part in this passive DMFC system. Concentrated methanol solution up to pure methanol has been used in this passive DMFC, and the cell produced attractive performance.
4. By using a porous hydrophobic membrane, we demonstrated gas removal from microchannel filled with 10M methanol. No leakage was observed at 0-30 psi of channel internal pressure. Breathing is achieved in any orientation. Based on the breathing mechanism, a bubble-breathing pump is proposed to replace external pump for fuel circulation. The proof-of-concept experiment verified the fuel circulation ability of this pump.
5. We performed micro channel experiments study the effects of wettability (hydrophilic/hydrophobic) as well as the presence of impurities in the fuel on the operating conditions of the device. We developed empirical correlations for the effective viscosity of a mixture of gas and either pure liquid or either liquid with impurities. The effective viscosity allows for the prediction of the energy requirement to drive the fuel in the fuel cells.
6. Numerical simulations were conducted for a liquid/gas mixer to study bubble transport in microchannels. The numerical results for bubble sizes as a function of channel width, liquid and gas flow rates, were in good agreement with experimental results. The grid independence study was completed and showed that the numerical simulations of bubble formation and transport are grid independent.

These research activities are described in more detail below.

Development of Advanced Membrane-Electrode Assemblies (MEA) and Micro DMFCs

A direct methanol fuel cell (DMFC) is an electrochemical cell that generates electricity based on the oxidation of methanol and reduction of oxygen. Fig.1 illustrates the cell construction and operating principle of a DMFC. The global oxidation reaction occurring at the platinum-ruthenium catalyst of the anode is given by:



Air is fed to the flow field on the cathode side. The oxygen in the air combines with the electrons and protons at the platinum catalyst sites to form water. The reduction reaction taking place on the cathode is given by:



The two electrochemical reactions are combined to form an overall cell reaction as:



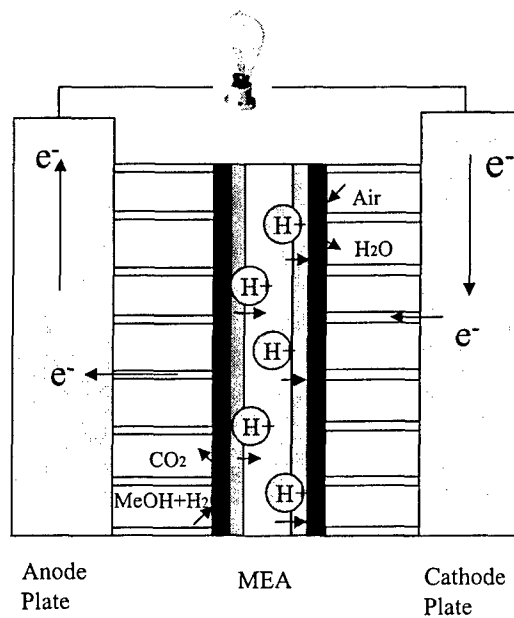


Figure 1: Schematic of a DMFC

The heart of a DMFC is a membrane-electrode assembly (MEA) formed by sandwiching a perfluorosulfonic acid (PFSA) membrane between an anode and a cathode. Upon hydrated, the polymer electrolyte exhibits good proton conductivity. On either side of this membrane are anode and cathode, also called catalyst layers, containing typically Pt-Ru on the anode side and Pt supported on carbon on the cathode side. These are where the half-cell reactions described in Equations (1) and (2) are catalyzed and take place. On the outside of the MEA, backing layers made of non-woven carbon paper or woven carbon cloth, as shown in Fig.2, are placed to fulfill several functions. The primary purpose of a backing layer is to provide lateral current collection from the catalyst layer to the ribs as well as the optimized gas distribution to the catalyst layer through diffusion. It must also facilitate the transport of water out of the catalyst layer. This latter function is usually accomplished by adding a coating of the hydrophobic polymer polytetrafluoroethylene (PTFE) to the backing layer. The hydrophobic character of the polymer allows the excess water in the cathode catalyst layer to be expelled from the cell by the gas flowing inside the channels, thereby alleviating flooding.

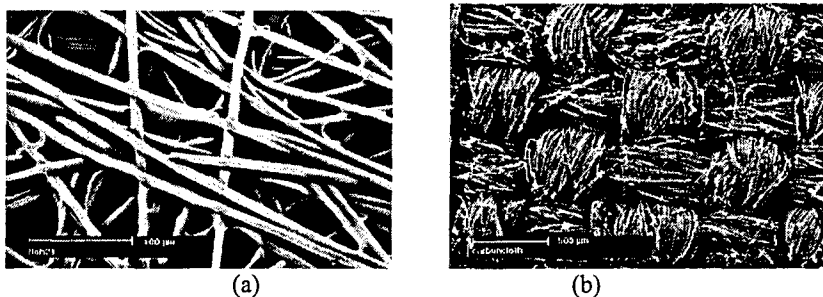


Figure 2: SEM micrographs of (a) carbon paper, and (b) carbon cloth

The microstructure of the catalyst layer is of paramount importance for the kinetics of an electrochemical reaction. Figure 3 shows scanning electron microscopy (SEM) pictures of such microstructures of the DMFC anode and cathode, respectively, where high surface areas for electrochemical reactions are clearly visible.

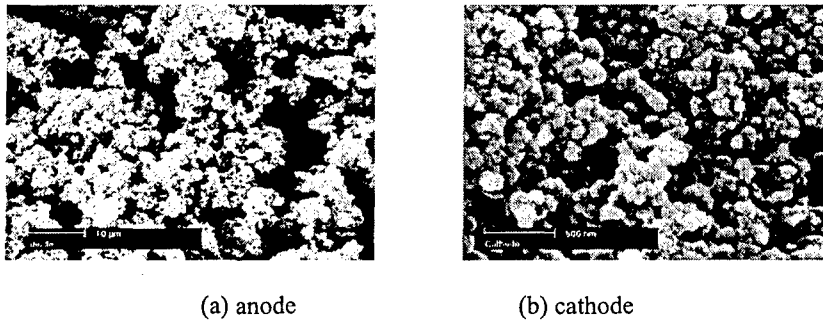


Figure 3: SEM pictures of electrodes

A cross-sectional SEM of a half MEA consisting of a backing layer, a microporous layer (MPL) and a catalyst layer, is displayed in Fig.4. The MPL with an average thickness of 30 μm is over a carbon paper backing layer. The anode catalyst layer of about 20 μm in thickness covers the MPL. In the anode, this MPL provides much resistance to methanol transport from the feed into the catalyst sites, thus reducing the amount of methanol crossover.

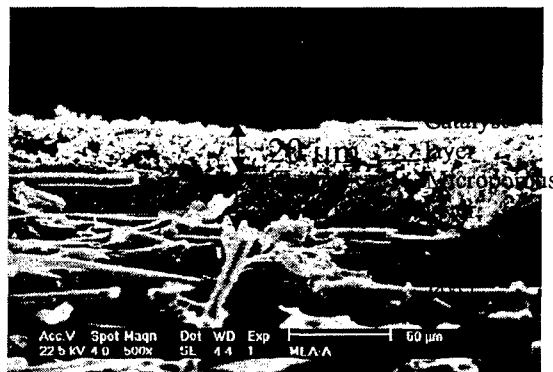


Figure 4: Cross-sectional SEM micrograph of backing layer, microporous layer, and catalyst layer.

Development of micro DMFCs

The μDMFC is fabricated by using silicon micromachining. A pair of silicon wafers with the thickness of 500±20 μm is employed as bipolar plates. The serpentine channels featured with three parallel partial cross-sections have been designed to mitigate the clogging of by-product CO₂ in the flow field. Deep reactive ion etching (DRIE) followed by photolithography process is applied to inscribe the fluid channels into Si wafers with 400 μm in depth. The second DRIE step is performed on the back side of the wafer to fabricate through-hole structures allowing methanol fuel to flow in and out. At this step,

double-sided aligned photolithography has been used to achieve the precise alignment between the fluid channels and the fuel feeding holes located on both sides of the wafer.

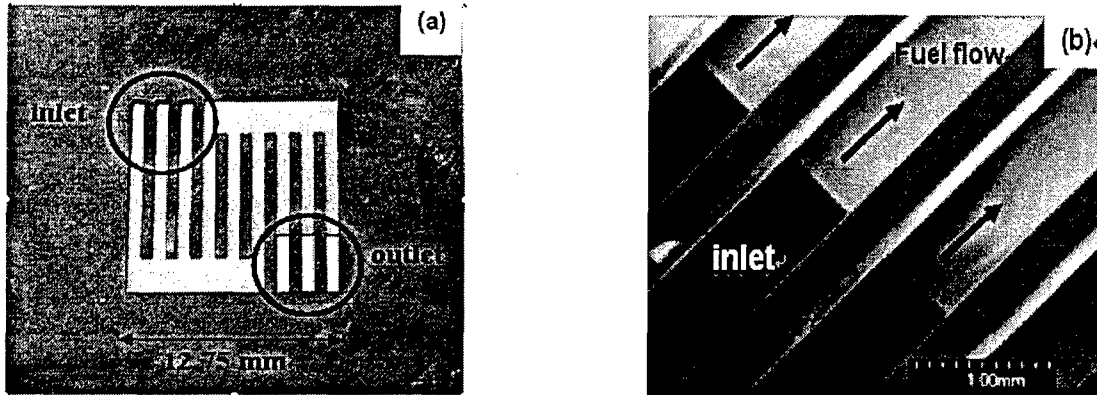
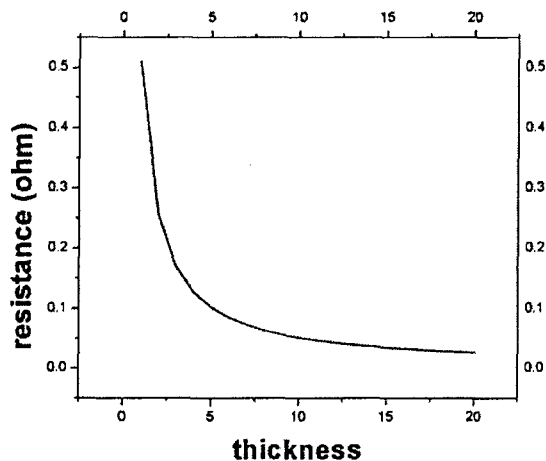


Figure 5: (a) Optical image of the Si-based bipolar plate. The detailed dimensions of the serpentine flowfield are 750 μm in width, 400 μm in depth and 12.75 mm in length. (b) SEM picture at the tubing area. It shows the details of the channels, exhibiting the well defined geometrical structure by two DRIE etching processes.

Next, to keep high energy conversion efficiency, how to decrease the electrical loss during operation becomes a very crucial issue for μDMFC project. The overall electrical resistance is described in equation (1), consisting of contact resistance and resistance from a conduction layer itself. In this case, we ignore the contact resistance. Assuming a microchannel of a 2.24 cm length and 0.07cm width, we can calculate the relationship between resistance and thickness as shown in Fig. 6. In accordance with this curve, 3 μm thick is the convincing number to acquire a low electrical loss conduction layer and feasible in fabrication.

Figure 6: Relationship of resistance and conduction layer thickness.



$$R_{tot} = R_{cont} + \frac{\rho_{cu} l}{t \cdot w}$$

Besides, methanol can erode most of metals gradually, so we must use gold as the conduction layer to avoid this problem. As a result, Ti/Cu/Au (0.01/3/0.5 μm) layers are deposited on the front-side of wafers by electron beam evaporation in order to collect the

generated current and to prevent whole conduction layer from methanol corrosion. In Fig. 7, the metallization result is shown and the cross-section of multilayer structure. Note that the electrical resistance is less than 0.1Ω everywhere measured by multimeter.

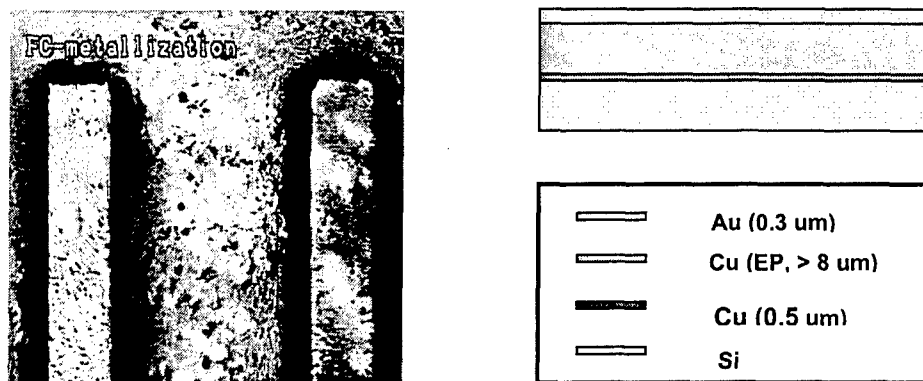


Figure 7: Optical microscopic picture of metallization result. We combine e-beam evaporation and electroplating to obtain thick conduction layer with gold finish.

Finally, to form a close channel for fuel flow two corresponding micromachined dies of microchannels are aligned together as shown in Fig. 8. Notice that these two dies are not symmetric, so they are not overlapped completely as shown in Fig. 9. In fact, we fabricate this layout on purpose because those open areas (orange part in Fig. 9) are reserved for the function of welding electrodes.

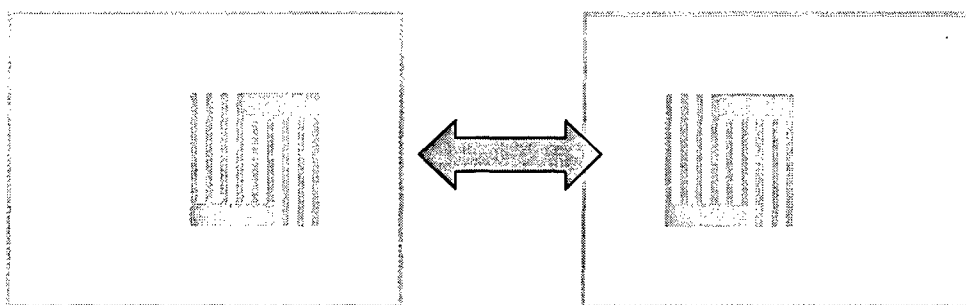


Figure 8: Illustration of packaging two corresponding micromachined dies to form a close channels for fuel flow .

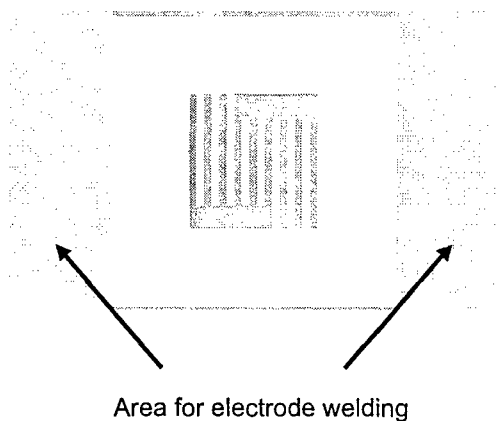


Figure 9: Open areas for welding electrodes on two ends of micromachined dies.

To measure the cell performance, we utilized a peristaltic pump to deliver the liquid fuel (1M aqueous methanol), with a feeding rate of 0.283 mL/min. A gas flow meter was also equipped to monitor an 88 mL/min air flow at room temperature. Meanwhile, an electric heater with temperature control was attached on the surface of the cell to investigate the cell output at different temperatures. An electronic load system (BT4, Arbin) was utilized to measure the relationship between cell voltage and current density (termed as polarization curve) in a galvanodynamic polarization mode at a scan rate of 3 mA/s.

Figure 10 shows a picture of the silicon wafer with fabricated flow channel pattern. The active area is 1.625cm^2 , with the flow channel and the rib separating two neighboring channels being $750\ \mu\text{m}$ wide, and the channel length of 12.75mm.

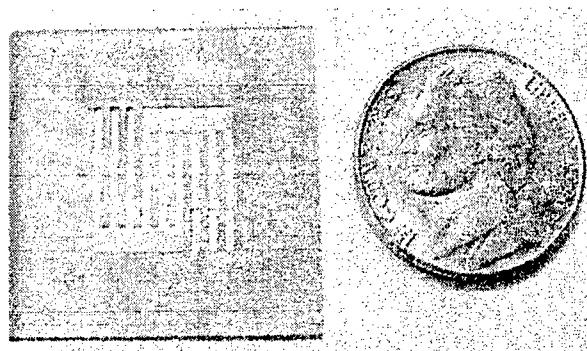


Figure 10: Picture of a silicon wafer with flow channels

Figure 11 shows a series of cell polarization curves operated at different temperatures using 1 M methanol solution under the ambient pressure. The maximum power density of the cell reaches $14.27\ \text{mW}/\text{cm}^2$ at a voltage of 0.196 V at room temperature (i.e., 23°C). The maximum power density is $24.75\ \text{mW}/\text{cm}^2$ at a voltage of 0.214 V when the temperature increased to 40°C . This is because the kinetics of electrodes, particularly methanol oxidation at the anode, are enhanced at elevated temperatures. For the same reason, maximum power density is $47.18\ \text{mW}/\text{cm}^2$ at a voltage of 0.258V and temperature of 60°C .

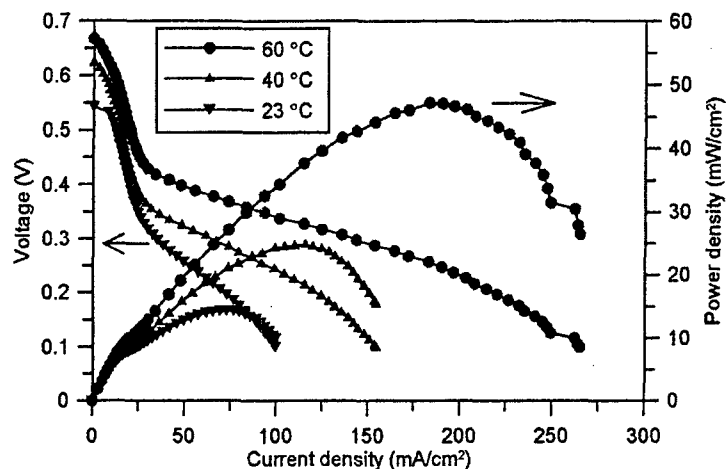


Figure 11: Polarization and power density curves at different temperatures using 1 M methanol solution with the air flow rate of 88 mL/min and methanol flow rate of 0.283 mL/min at atmospheric pressure.

Figure 12 displays polarization curves of the micro DMFC for different temperatures under ambient pressure using 2 M methanol solution with feed rates of 88 mL/min on the cathode side and 0.283 mL/min on the anode side. The maximum power density of the micro DMFC at 2M, however, reaches: 50 mW/cm² at 0.2V and 60°C; 33 mW/cm² at 0.17 V and 40°C; and 16.5 mW/cm² at 0.14V at room temperature.

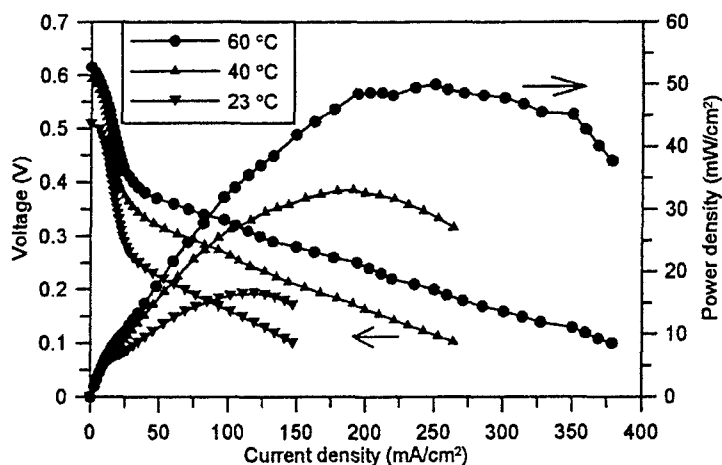


Figure 12: Polarization and power density curves at different temperatures using 2 M methanol solution with the air flow rate of 88 mL/min and methanol flow rate of 0.283 mL/min at atmospheric pressure.

An alternative method to fabricate the bipolar plate was proposed using photochemical etching of thin stainless steel plates (500 μm or thinner) for μDMFCs instead of silicon wafer and ceramic. Stainless steel has much higher conductivity and mechanical strength. A thin layer of gold coating on stainless steel plate is sufficient to prevent corrosion and improve the electric contact. A μDMFC fabricated by photochemical etching has been

developed, with effective area of 1.625 cm^2 , and with the same flow pattern and effective area as the Si-based micro DMFC we reported earlier.

Figure 13 shows the polarization curve and power density using 2 M methanol solution at 22°C and atmospheric pressure. The methanol flow rate is 2.2 mL/min , and the air flow rate is 161 mL/min . The current density reaches 90 mA/cm^2 at 0.3 V and the maximum power density is 34 mW/cm^2 at 0.23 V . This is much better than our previous results using Si-based μDMFC where the maximum power density at 23°C and atmospheric pressure was 16.5 mW/cm^2 at 0.14 V .

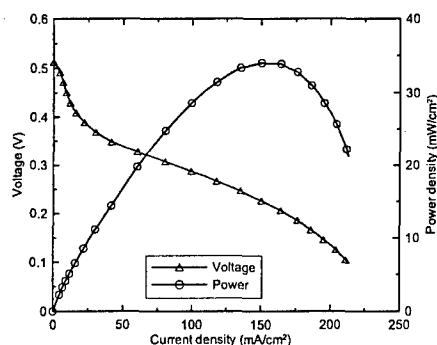


Figure 13: Polarization curve using 2 M methanol solution at 22°C , with air flow rate of 161 mL/min , methanol flow rate of 2.2 mL/min , and ambient pressure.

Figure 14 depicts the polarization curves and power densities using 2 M methanol solution at 40°C and atmospheric pressure. The cell performance reaches about 200 mA/cm^2 at 0.3 V and the maximum power density is 62.5 mW/cm^2 at 0.26 V . This is a significant improvement compared to the previous maximum power density of 33 mW/cm^2 at 0.17 V in the Si-based μDMFC .

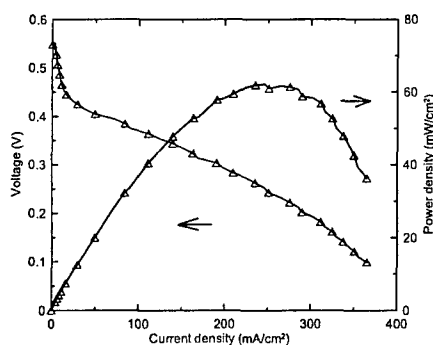


Figure 14: Polarization curve using 2 M methanol solution at 40°C , air flow rate of 161 mL/min , methanol flow rate of 2.2 mL/min , and ambient pressure.

Figure 15 shows the polarization curves and power densities using 2 M methanol solution at 60°C and atmospheric pressure using different air flow rates. The methanol flow rate was fixed at 2.2 mL/min . At low current density, the cell voltages are almost identical at different air flow rates. The overall cell performance becomes better with increasing air

flow rate. With the air flow rate of 375 mL/min, cell performance reaches 330 mA/cm² at 0.3 V and the maximum power density is 100.2 mW/cm² at 0.28 V. This is much higher than 50 mW/cm² at 0.2 V and 60 °C for the Si-based μ DMFC.

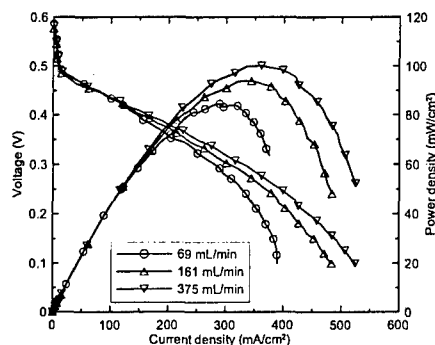


Figure 15: Polarization curve using 2 M methanol solution at 60 °C at different air flow rates, methanol flow rate of 2.2 mL/min, and ambient pressure.

Flow visualization in the DMFC

Figure 16 shows a picture of the transparent fuel cell. The cell is constructed of a pair of stainless steel plate mated with a polycarbonate plate. A total of eight (8) parallel flow channels (1.92mm width, 1.5mm depth, 1mm rib width) were machined through the stainless steel plate to form an effective area of approximately 5cm². The surface of the stainless steel plate contacting the MEA was coated with 30nm Cr and 300nm Au to minimize contact resistance. A transparent polycarbonate plate covered the stainless steel plate, forming a window to allow direct observation of flow behaviors. The polycarbonate plate was concave in design, while the stainless steel plate had a matching convex pattern. This unique design avoided flow leakage between neighboring parallel channels. Cell inlet and outlet manifolds were also machined in the polycarbonate plates.

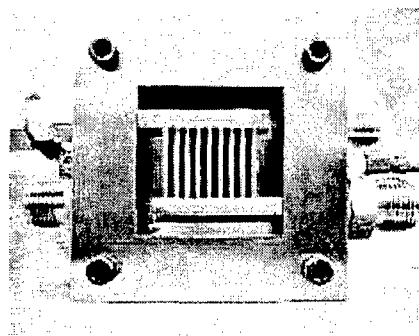


Figure 16: Photo of the transparent fuel cell

Figure 17 shows a sequence of images at various times for ECEC MEA at the feed temperature of 85°C and the current density of 100mA/cm². The images, one second

apart, were captured from the movie, with time resolution 1/30 second. In addition, the time of the first image was chosen arbitrarily due to the fact that two-phase flow is a regularly periodic event. As shown in Fig.17, the CO₂ bubbles nucleate at certain locations and form large and discrete gas slugs in the channel. The bubble motion is governed by the momentum of liquid flow, the force of buoyancy on the bubble, and the surface adhesion between bubbles and substrate. It can be seen from Fig.17 that bubbles are held on the carbon paper by strong surface tension until they grow into larger slugs for detachment, clearly indicative of the dominant effect of surface tension in bubble dynamics in DMFC. Once the bubbles grow to a sufficient size, they detach and sweep along the backing surface in the channel. This sweeping process clears all small bubbles pre-existing on the backing surface, making new bubbles grow from the smallest size to the full detachment diameter. As a result, the two-phase flow becomes regularly intermittent.

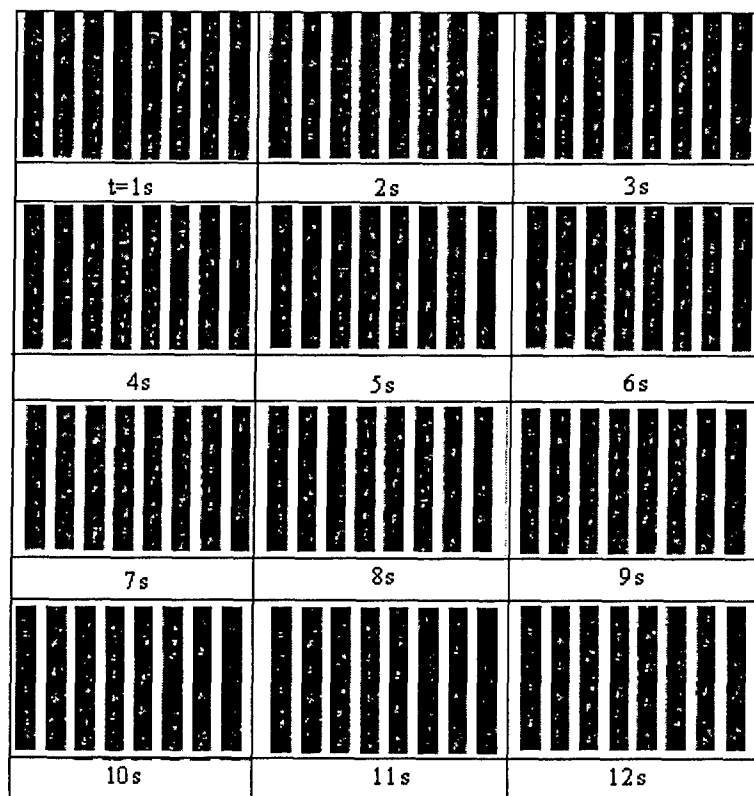


Figure 17: Images of bubble dynamics in the DMFC anode using ECEC MEA (carbon paper) for 2M MeOH feed (20.8mL/min and 0 psig) and non-humidified air (700 mL/min and 15 psig) at 100 mA/cm² and 85°C.

Water management in the DMFCs

For each mole of methanol, one mole of water is needed for methanol oxidation at the anode and roughly 2.5×6 moles of water are dragged through a thick membrane such as Nafion 117 towards the cathode, assuming that the electro-osmotic drag coefficient of water is equal to 2.5 per proton [12]. This then causes 16 water molecules lost from the anode for every mole of methanol. Water in the anode therefore must be replenished. On the other hand, in the cathode there are 15 water molecules transported from the anode and additionally 3 water molecules produced by consuming 6 protons generated from oxidation of one methanol. Presence of a large amount of water floods the cathode and reduces its performance. The difficult task of removing water from the cathode to avoid severe flooding and supplying water to the anode to make up water loss due to water crossover through the membrane is referred to as innovative water management in a portable DMFC.

Figure 18 shows a picture of the experimental setup. The effective area of the DMFC test fixture is 5cm^2 . A digital pump (Series I digital pump, Laballiance) with the range of $0.01\text{mL}/\text{min}$ - $10\text{mL}/\text{min}$ was used to deliver methanol aqueous solution and control its flow rate. 2M methanol solution was employed to test the cell performance in this work. A digital mass flow controller (Omega Engineering, Inc) was used to measure and control the flow rate of non-heated and non-humidified air. A digital temperature controller was used to control the electric heater on the cell to maintain the desired cell temperature. A water moisture trap containing anhydrous calcium sulfate (W. A. Hammond Drierite Co. LTD) was connected to the exit of the cathode to collect water in the effluent. An electronic load system (BT4, Arbin) in the galvanodynamic polarization mode was used to measure polarization curves at a scan rate of $3\text{mA}/\text{s}$.

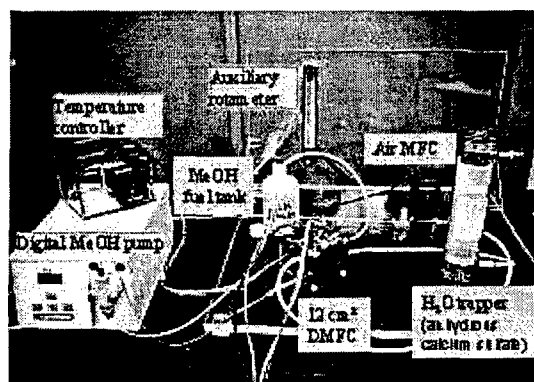


Figure 18: Schematic of experimental setup

We have developed a new MEA which enables to reduce the net water transport coefficients significantly based on a new water management technique. Figure 14 displays the net water transport coefficient α measured at different temperatures using our new MEA. It is seen from Fig.19 that the net water transport coefficient α increases with temperature nearly exponentially. This is because the water vapor saturation pressure in the cathode increases sharply with temperature, thereby promoting water

removal through the cathode air. It is seen from Fig.19 that α is only 0.05 at room temperature, 0.16 at 40°C, and 0.64 at 60°C, respectively. This range of α is significantly lower than the pure electro-osmotic drag coefficient.

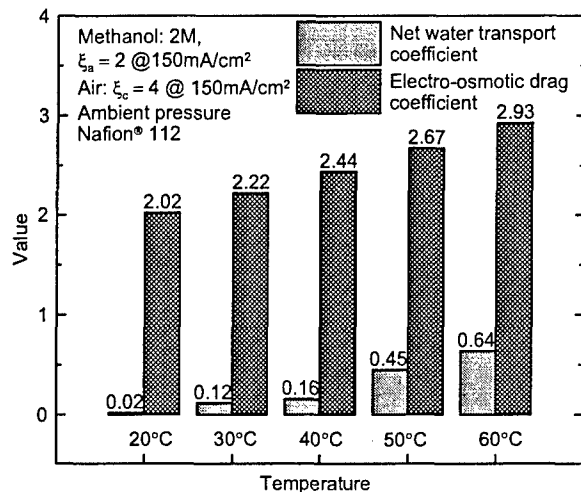


Figure 19: The net water transport coefficient α at different temperatures compared to electro-osmotic drag coefficient

Development of an 8-cell Air-breathing DMFC stack

Stainless steel plates with a thickness of 500 μm were used as bipolar plates to collect current. Flow channels were fabricated in the plates by photochemical etching method. The effective area of each cell was 5 cm^2 and total gross area was 33 mm \times 33 mm. In order to minimize contact resistance and prevent corrosion, a gold layer of 300 nm in thickness was deposited on the interior side of each stainless steel plate. A rectangular polycarbonate plate (145 mm \times 33 mm \times 5.6 mm) was fabricated with liquid feeding channels to support 8 individual cells (4 cells on each side). The gross volume of this 8-cell stack is about 34 cm^3 . Figure 20 shows the flow path arrangement for the 8-cell stack. The flow paths are parallel with the length of each flow channel being equal to ensure uniform flow distribution to each cell.

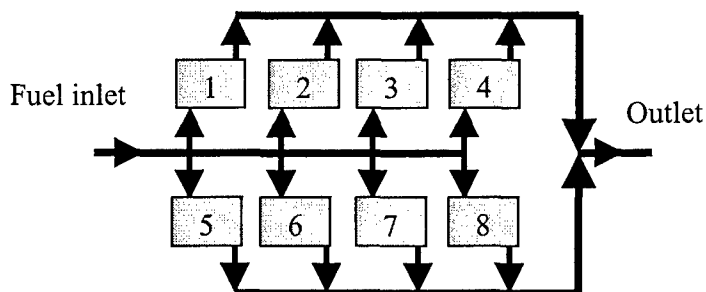


Figure 20: Parallel flow paths for eight cells in a stack

Figure 21 depicts the voltage distribution for the 8 individual cells at three different current densities at steady state by fixing the current density. The little difference between the performance of cell 1 and cell 5, as well as between the performance of cell 2 and cell 6, might be due to flow mal-distribution. It is seen from Fig. 2 that the average voltage at steady state by fixing the current density reached 0.42 V at 25 mA/cm², 0.38 V at 50 mA/cm², and 0.33 V at 75 mA/cm², respectively.

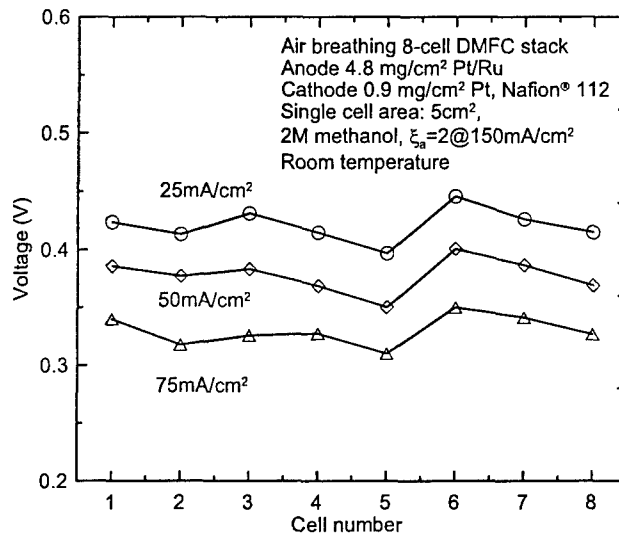


Figure 21: Voltage distribution in the 8-cell stack

Figure 22 shows the polarization curve for the 8-cell stack. The cells were connected in series. The stack produced 1.28 W at 2.4 V and the maximum output power was 1.33 W at 2.21 V, corresponding to a power density of 33.3 mW/cm². Figure 23 displays the stack voltage curve discharged at a current of 375 mA. The stack voltage was found to be higher than 2.54 V (an average of 0.3175 V for each cell) with a steady-state power output of 23.8 mW/cm² produced for more than 100 mins without significant decay.

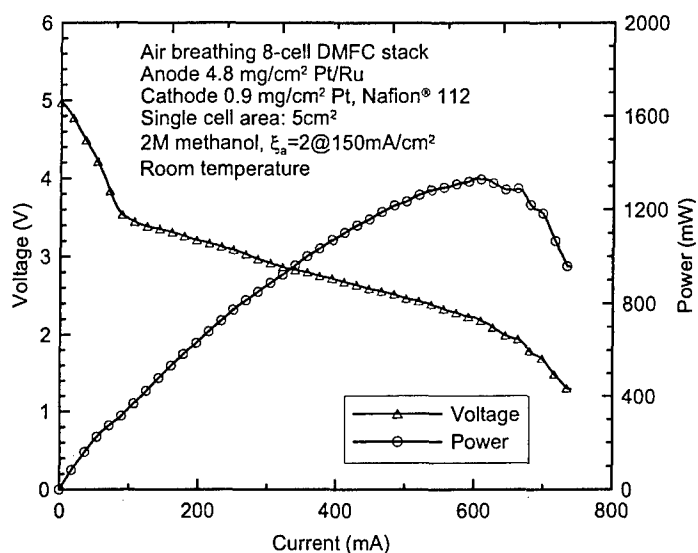


Figure 22: Polarization and power curves of the 8-cell air-breathing DMFC stack

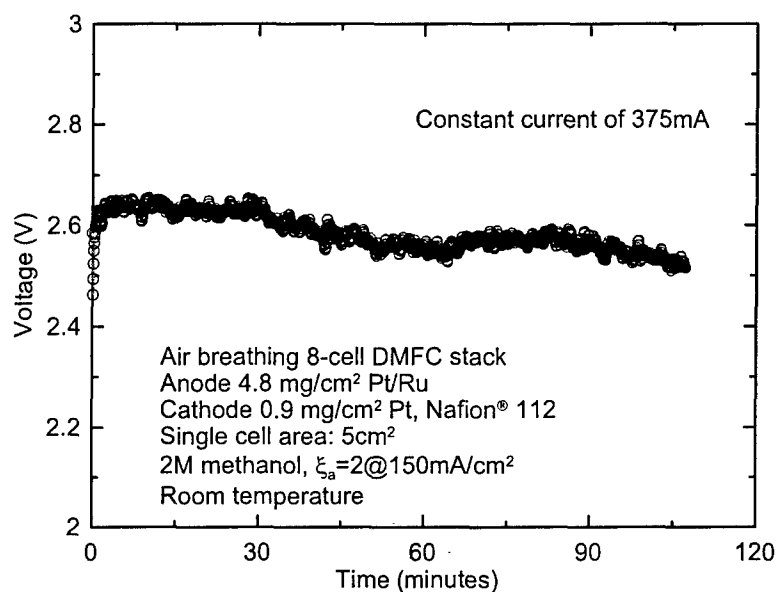


Figure 23: Discharge curve of the DMFC stack at constant current of 375 mA

Development of passive DMFCs using pure methanol

Experimental demonstration of a passive DMFC using 17 M methanol solution and pure methanol has been carried out. The passive DMFC produced a steady-state power output of 21 – 27 mW/cm² using pure methanol over 15 hours at near room temperature. Figure 24 shows the discharge performance of this passive DMFC using 17 M methanol solution under a current load of 100 mA/cm². The voltage keeps higher than 0.27 V over 5 hours without significant performance decay, which produces a steady-state power output of 27 mW/cm².

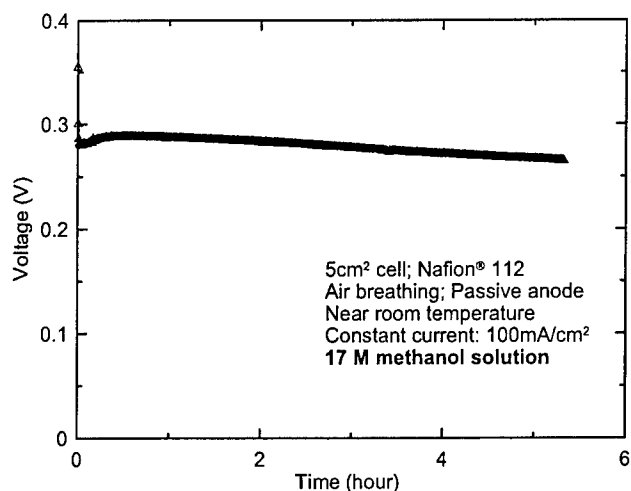


Figure 24: Reliability of a 5cm² passive DMFC operating with 17 M methanol solution

Figure 24 depicts the discharge performance of the passive DMFC using pure methanol in the anode, with a current load of 100 mA/cm². The cell temperature is still around 28°C. Shown in Fig.25, the voltage increases with time at the beginning of discharge and then gradually decreases. The range of the voltage varies from 0.27V to 0.21V over a period of more than 10 hours, which produces a steady-state power output of 21 –27 mW/cm².

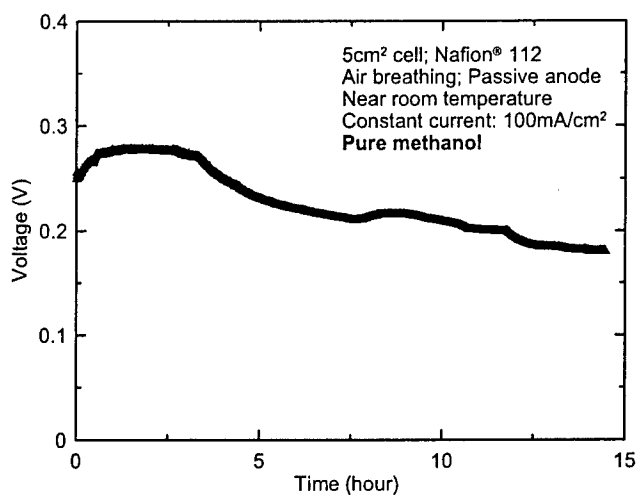


Figure 25: Reliability of a 5cm² passive DMFC operating with pure methanol at near room temperature

Distributed Gas Breather Design

By using hydrophobic nanoporous membrane, we have demonstrated gas removal from microchannel filled with 10M methanol. No leakage was observed at 0-30 psi of channel internal pressure. Breathing is achieved in any orientation. Based on the breathing mechanism, a bubble-breathing pump is proposed to replace external pump for fuel

circulation. The proof-of-concept experiment verified the fuel circulation ability of this pump.

Hydrophobic nanoporous venting

Using the distributed breathing concept, proven in the previous research, we have verified that the growth of gas bubbles in liquid can be kept under check. Performance of the μ DMFC will be greatly improved if gas bubble contents in microchannels are limited because: (1) flow resistance through microchannels is decreased, (2) active electrode area is increased, (3) discrete gas separator is eliminated, and (4) liquid exposure area is reduced to minimize fuel evaporation loss. Fig. 26 shows that a hydrophobic breathing hole can support a liquid meniscus in it so as to withstand some transmembrane pressure without losing liquid by leakage. As shown in Fig. 26, the transmembrane pressure difference across the meniscus is:

$$P_f - P_o = \frac{2\sigma_f \cdot \cos(\pi - \theta)}{r} \quad (1)$$

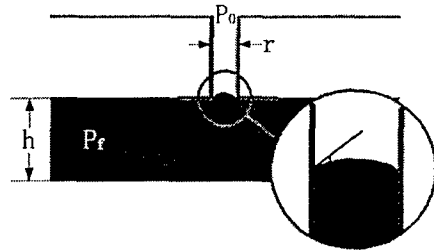


Figure 26: Transmembrane pressure for a simplified single breathing hole

When θ reaches its maximum value (advancing contact angle θ_a), the transmembrane pressure also reaches its limit. If the inside liquid pressure increase further, leakage will happen. So, the leakage pressure of such a simplified single hydrophobic breathing hole is:

$$P_{leak} = \text{Max}(P_f - P_o) = \frac{2\sigma_f \cdot \cos(\pi - \theta_a)}{r} \quad (2)$$

Hydrophobic nanoporous membrane has been identified to improve leakage onset pressure, because of their nanometer-sized hole size and intrinsic hydrophobic material. The real condition for a hydrophobic nanoporous membrane can be much more complex. If the topology of breathing hole is considered, the leakage pressure of each breathing hole should be determined by its most constrict neck, in term of effective radius $r_{effective}$. The surface morphology can also change the contact angle to effective contact angle $\theta_{effective}$. Both of them contribute to the maximum pressure that this breathing hole can withstand. In membrane scale, the leakage should be attributed to the pore which is most susceptible to it. Then the leakage pressure of a porous membrane can be described as:

$$P_{leak} = \text{Min} \left(2\sigma_f \cdot \text{Max} \left(\frac{\cos(\pi - \theta_{effective,adv})}{r_{effective}} \right) \right) \quad (3)$$

The leakage onset pressure is measured by observing the flow rate while increasing pressure gradually in a dead-end micro-chamber covered by hydrophobic nanoporous membranes. The results are summarized in Table 1.

Table 1. Leakage onset pressure

	Polypropylene	PTFE A	PTFE B
10M Methanol	> 35 psi *	~5 psi	~ 4 psi
DI water	>35 psi *	16 psi	16 psi

* membrane broke at about 35 psi

Fig. 27 shows the venting process of a single gas bubble in a venting-membrane-covered microchannel filled with 10M methanol.

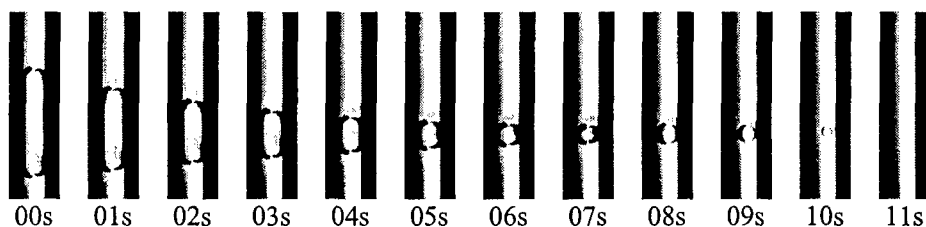


Figure 27: Reducing of a single bubble in 10M Methanol by hydrophobic venting

The breather showed ability to breath out CO_2 quickly in high concentration methanol, which can enable an efficient pumping mechanism because the efficiency of most reported micro bubble pump are limited by bubble reducing step, where condensing of vapor bubble is usually employed. Moreover, the CO_2 bubble produced by electrochemical reaction in μDMFC is obvious a convenient resource for bubble pump to delivery fuel.

The general pumping concept is schematically described in Fig. 28. To simplify the analysis, a pumping cycle with a single bubble is divided into three steps: (1) When a bubble grows at a location close to the virtual check valve of a microchannel, expansion of the meniscus is hindered by the check valve on the left. Consequently, the bubble only grows to the right and pushes the liquid rightward. (2) The shape of hydrophilic microchannel can be designed to promote rightward bubble motion. A diverging shape microchannel is specified here, However, pumping is also observed in a simple straight channel. Therefore the diverging channel design can help, but is not required, to complete the pumping. The design of the channel shape can be further optimized to improve the pumping performance. Another factor that facilitates the rightward motion of bubble is the surface free energy difference between hydrophilic channel wall (SiO_2) and hydrophobic membrane. This energy gradient makes the membrane a “bubble trap” (as discussed in chapter 2), which attracts the gas bubble to it automatically. Therefore, the bubble is drawn into the membrane region once it reaches the hydrophobic nanoporous membrane. (3) Through the breathing holes in the membrane, the bubble is vented out without any liquid loss, providing a pressure difference ($P_l - P_0$) less than P_{leak} (e.g. ~35psi for the device thereby). The liquid then fills into the section symmetrically to replace the

vacancy left by the gas bubble. A pumping cycle is thus completed and a net pumping to the right is achieved.

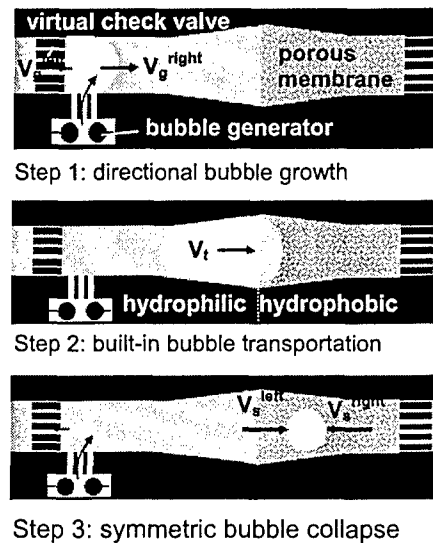


Figure 28: Pumping by directional growth and hydrophobic venting of gas bubbles: the concept

Although this concept is illustrated with a single bubble, the coexistence of multiple bubbles is acceptable for pumping as long as the venting rate of the membrane is sufficient to remove all the bubbles promptly. Therefore, continuous bubble generation can be used for the bubble-driven micropump reported here. Tolerance of bubble generation pattern enables the pump's applications in μ DMFC.

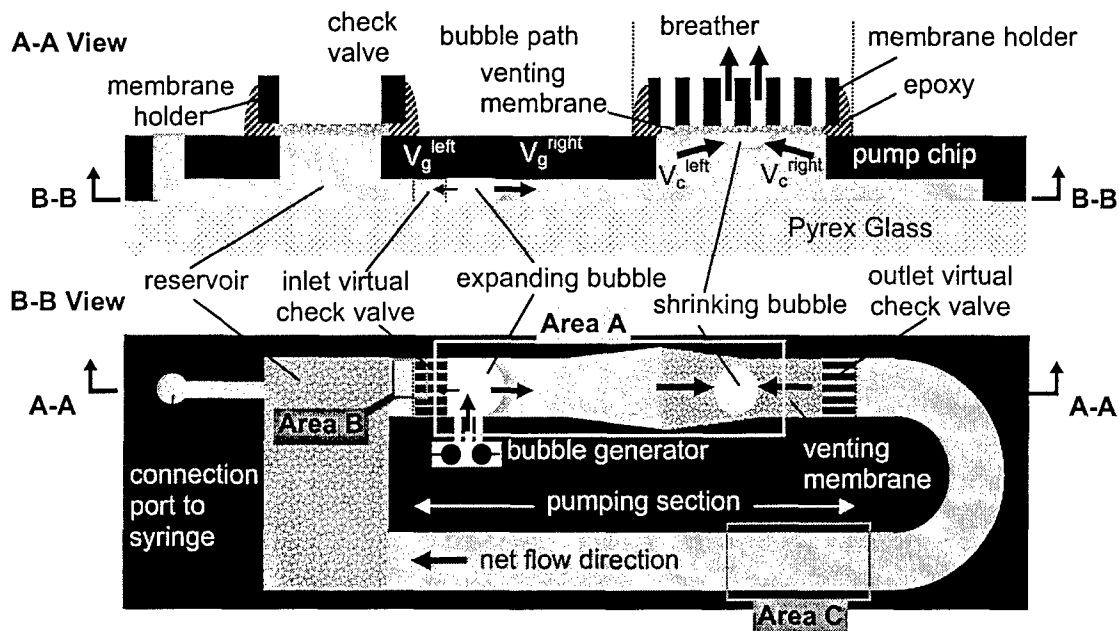


Figure 29: Bubble-driven pump loop enabled by hydrophobic venting

A bubble-driven pump loop is constructed as Fig. 29 shows, so as to verify continuous liquid circulation in μ DMFC. The elimination of open ends also prevents some uncertainties about the device, such as evaporation and the pressure effect of the menisci. The pump chip and membrane holders are all fabricated from the same 400 μ m-thick <100> silicon wafer by DRIE etching. On the pump chip, the microchannels of the breather, the reservoir and the connection port are etched through. Other parts of the pump loop are protected by polyimide tape once the DRIE etching has reached the desired depth. After DRIE and subsequent Piranha cleaning, the pump chip is anodically bonded to a piece of Pyrex[®] glass. Then the venting membranes are sandwiched between the pump chip and membrane holders. They are bonded together by epoxy adhesive to form a breather. Two platinum wires are inserted into the “bubble source” position as the electrodes for electrolysis. The finished pump loop (as illustrated in Fig. 30) is subsequently connected to a syringe via a tubing/fitting/adaptor apparatus.

The working fluid, Na₂SO₄ aqueous solution (~0.2M), is filled into the finished device through the syringe. In order to verify the liquid circulation more concretely, the fluid uptake from the reservoir was observed in area B of Fig. 29. Fluorescent particles (4 μ m in diameter) are mixed into the working fluid to visualize the flow. Figure 30 shows the video sequence of fluid uptake captured by a fluorescent microscope. The flow close to the inlet of the check valve was found to be essentially unidirectional with occasional stops. Unidirectional fluid uptake implies that fresh fuel from the reservoir of μ DMFC can be supplied to the anodic channel by using this pumping approach.

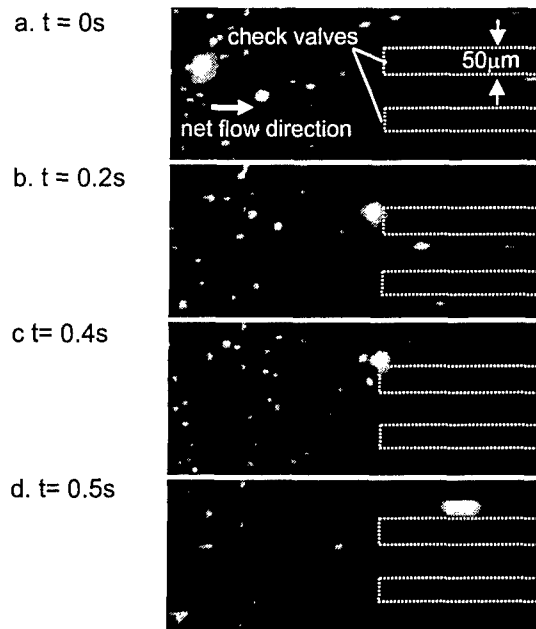


Figure 30: Fluid uptake from the reservoir

Liquid-gas multiphase flow in microfluidic devices for μ DMFCs

Fluidic management in Direct Methanol Fuel Cells

Multiphase flow occurs in many operations in the chemical, petroleum, and power generation industries (such as nuclear power plants and micro fuel cells). Unlike large-scale systems, gas bubbles can present significant problems in microfluidic systems by disturbing and eventually blocking the flow. Interactions on the boundaries between gas, liquid, and solid introduce nonlinearity and instabilities. Understanding how bubbles affect the flow resistance in microchannels is, beside its fundamental aspect, a concern of determining the pumping or energy requirement for portable microfluidic devices where two-phase flow is involved such as in a micro Direct Methanol Fuel Cell (μ DMFC). The objectives of the work reported in following sections are to understand the conditions necessary to purge gas bubbles from square microchannels. We report investigations on the wedging effect and two-phase flow transport phenomena in microchannels with surface modifications. We first study the shape of a static elongated bubble in microchannel as a function of the contact angle. Then, we characterize a bubble generation process in microchannel as a function of operating parameters. This bubble generation process is used to study liquid/gas flow in different geometries at the microscale. This study provided many insights on micro-multiphase flows, in particular, we compare multiphase flow made of pure liquid and gas and multiphase flow made of a mixture of liquid with surface active agent, that can be seen as impurities, and air. We performed these study in hydrophilic and hydrophobic channels.

Static capillary shape confined in polygonal microchannels

The shape of a static elongated bubble in a N -sided regular polygonal capillary depends on N and the contact angle θ . When $\theta < \pi/N$, liquid fills the channel wedges, and when $\theta > \pi/N$, gas fills the entire channel cross-section. Figure 31 displays experimental pictures of a static elongated gas bubble in a square capillary. The black color represents a large liquid/gas curvature. The contact angle θ is the boundary condition that sets the shape of the liquid/gas interface. In the transition from partially non-wetting surfaces ($\theta > \pi/2$) to partially wetting surface ($\theta < \pi/2$), there is an inversion of the sign of the liquid/gas curvature (Figure 31, a and b). When $0 < \theta < \pi/4$, the bubble does not fill the wedges of the channel (Fig. 31. c). The system lowers its energy by creating a triple line (liquid/solid/gas); and gas directly contacts the center of the channel walls where small liquid droplets may be present. For a completely wetted system ($\theta = 0$), the gas bubble is lubricated by a liquid film (see Fig. 31. d).

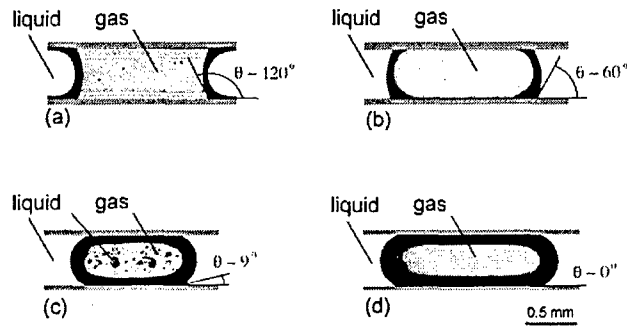


Figure 31: Shapes of static bubble in square microchannel for different contact angles. (a) hydrophobic plug bubble, (b) hydrophilic plug bubble, (c) wedging bubble with contact line, (d) lubricated bubble.

When motion is induced, contact angle hysteresis increases the complexity of the system. Velocity increases the advancing contact angle and decreases the receding contact angle, causing the bubble to lose symmetry with respect to the direction of the flow. Since contact angles are influenced by roughness and heterogeneities of the solid surface, moving bubbles may lose their symmetry with respect to the center axis of the channel. We experimentally investigated flow patterns when liquid and gas are flowing into square cross-sectional microchannels. The optimal wettability properties for Micro-Direct Methanol Fuel Cells are hydrophilic in the anode channel in order to reduce flow resistance to push gas bubbles and hydrophobic in the cathode channel in order to reduce flow resistance to push liquid droplets.

Experimental set-up

A. Microchannels fabrication

Channels are made with glass and silicon using microfabrication techniques. Channel masks are printed in positive with a high-resolution printer on transparent paper for lithography. Photoresist is spin coated on a 10 cm double-sided polished silicon wafer. The wafer is then exposed to UV light through the mask. The parts of the resin layer exposed to UV light are removed by immersion in a developer bath. Channels are etched at different depths using Deep Reactive Ion Etching (DRIE). The sealing is made with Pyrex glass using anodic bonding, providing optical access for flow analysis. Flexible tubes are glued with epoxy on gas and liquid inlets and on the pressure sensor inlet.

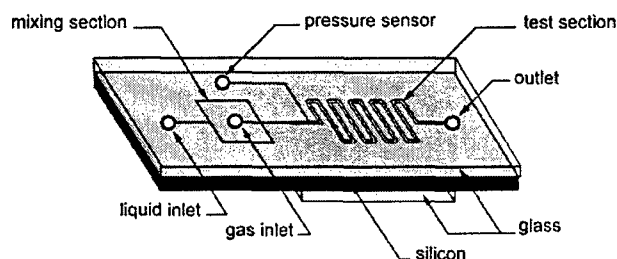


Figure 32: Two-phase flow microchannel module: Mixing section (50- μ m square channel), Test section (200- or 525- μ m square channel).

Figure 32 shows a typical channel module. Channels are composed of two parts: a mixing section ($50 \pm 5 \mu\text{m}$ square channel) and a test section (200 ± 10 or $525 \pm 10 \mu\text{m}$ square channel). A $50\text{-}\mu\text{m}$ square channel is connected to the main channel to allow pressure measurements. Experiments were conducted using DI water and air. As channels were partially wetting, contact angle hysteresis was measured using DI water droplets on progressively tilted surfaces. Advancing and receding contact angles were measured on glass and on DRIE silicon just before the droplet started moving. The advancing contact angle on glass is $\theta_{a,\text{glass}} = 25^\circ \pm 1^\circ$ and the advancing contact angle on DRIE silicon is $\theta_{a,\text{silicon}} = 9^\circ \pm 1^\circ$. The receding contact angle for both glass $\theta_{r,\text{glass}}$ and silicon $\theta_{r,\text{silicon}}$ were slightly above 0° . Dewetting phenomena were observed in the experiments confirming the non-strictly zero receding contact angles.

B. Apparatus

A schematic diagram of the experimental apparatus is shown in Figure 33. Liquid is injected into the channel from a reservoir, the pressure of which is adjustable with a miniature regulator. The liquid flow rate Q_L is measured at the channel inlet with a liquid volumetric flow meter (from 0 to 1 ml/mn). Gas is coming from a compressed air tank, the pressure of which is also adjustable with a miniature regulator. Air flow rate Q_G is measured with gas mass flow meters (form 0 to 100 ml/mn). Mass flow meters determine the volumetric flow rate at the channel outlet based on the viscosity of the air at the measured temperature. The pressure inside the test channel is measured with a differential pressure sensor ranging from 0 to 1, 5 or 15 psi depending on the flow rate. Before each measurement, the pressure sensor channel is flushed with water to remove all trapped air pockets. After each change of the gas inlet pressure, the system was allowed to reach a steady state. The steady state is defined when pressure sensors, flow meters and bubble distribution are stationary. The measured pressure is averaged over 1000 points during 20 seconds. The liquid inlet pressure was limited to 50 psi ($\approx 3.4 \text{ Atm}$). Because of the large pressure drop in the mixing channel section, limiting the range of liquid flow rate in the main channel, the maximum two-phase pressure drop measured in the test section presented in this paper is about 9 psi ($\approx 0.6 \text{ Atm}$) for the dry flow, so that compressibility effects of gas are not significant since flow patterns and bubble size are uniformly distributed along the channels. In that case, a linear pressure distribution along the channel is assumed.¹⁶

A pressurized liquid reservoir was chosen instead of a mechanical syringe pump to allow the system to reach steady states. The channel outlet is permitted to vent directly into the atmosphere. A high-speed camera (10,000 fps) used with a 60 mm lens mounted on an extension tube is set above the channel to allow flow analysis. As channels are transparent, the light source (fiber light) is placed at the other side of the channels.

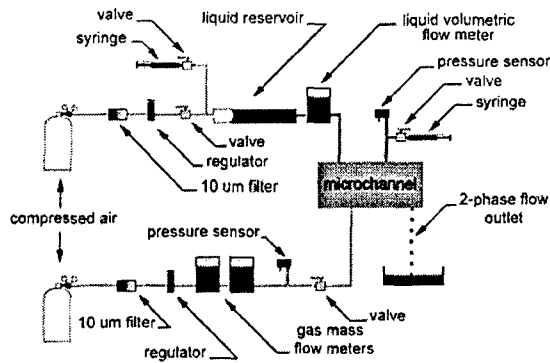


Figure 33: Experimental apparatus.

Multiphase flow production: bubble generation process

Figure 34 represents processed experimental pictures of a water/air mixer in 100 μm square channels for different liquid and gas superficial velocities J_L and J_G ($J_i = Q_i / h^2$, where h represents both channel width and height). Gas flows in the central channel and liquid is injected from the side channels. Bubble size and distribution are a function of the liquid and gas flow rates.

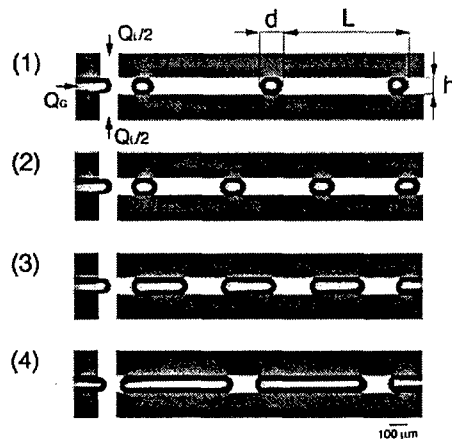


Figure 34: Bubble formation for different water and air superficial velocities. Liquid inlet pressure was kept constant while gas inlet pressure was increased.

The homogeneous liquid fraction $\alpha_L = Q_L / (Q_L + Q_G)$ is a relevant parameter to characterize liquid/gas flow in microchannels. For different sets of liquid and gas flow rates, we measured the bubble length d and the length L between bubbles using image processing. We plotted, Fig. 35., the bubble length d normalized by the channel width (and height) h , as a function of the homogeneous liquid fraction α_L . Experimental results performed with adding surfactant to the water do not depart from those performed without surfactant, suggesting that this phenomenon is relatively independent of surface tension over the range investigated. In both cases, the bubble length d follows a simple relationship, which can be expressed as follows

$$d = h\alpha_L^{-1}.$$

(1)

This expression can be analytically deduced by considering the time T necessary for the liquid to pinch the core gas bubble: $T = h/J_L = h^3/Q_L$. The bubble length d can be estimated by $d = V_B T$, where $V_B = (Q_L + Q_B) / h^2$ is the average bubble velocity. One should note that Eq. (1) is specific to the square channel geometry. Indeed, this geometry allows symmetries in the system and minimizes the surface area for a rectangular shape. It is particularly interesting to consider that the compact confinement of a capillary surface at small Bond number allows for its selective break-up according to a “geometric” law. The relative independence from surface tension can be understood by the fact that the capillary pressure is negligible compared to the pressure drop generated by the flow.

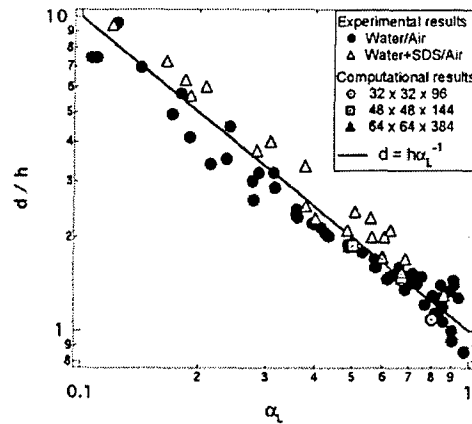


Figure 35: Bubble length d as a function of homogeneous liquid fraction α_L .

The bubble distribution is customizable using the distance L between the bubbles. The shape of a flowing elongated bubble in a square microchannel differs considerably from a cylinder. The film thickness between the bubble and the solid walls depends on the capillary number Ca , as well as the quantity of liquid in the corners. Due to viscous friction, in presence of surfactant, it is accumulated at the rear of the bubble, inducing a gradient of surface tension responsible for a slight bubble deformation compared to the non-surfactant case. In both cases, a first order approximation would neglect the bubble curvature, as well as the liquid flowing in the corner and in the thin film. By doing so, the bubble shape can be assumed as a rectangular plug of volume dh^2 . This approximation allows estimating the distance L between bubbles by writing $1 - \alpha_L = d/L$ combined with Eq. (1). The distance L between bubbles can be expressed as a function of the bubble length d , $L/h = (d/h)^2 / (d/h - 1)$. As can be seen in Fig. 36, experimental data agree fairly well with the prediction for large bubble length $d > 4h$. The distance between bubbles is minimal when the liquid flow rate equals the gas flow rate ($Q_L = Q_G$), corresponding to a bubble length $d/h = 2$. At this point the liquid length between the bubbles is equal to the bubble length.

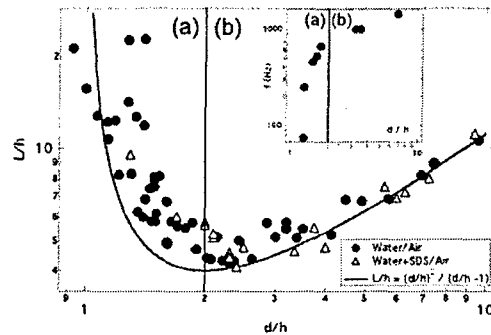


Figure 36: Evolution of the distance L between bubbles as a function of bubble length d .
Region of bubble formation: (a) pseudo constant volume and (b) pseudo constant frequency.

The bubble formation presented in this letter is somewhat analogous to the classical problem of bubble formation at an orifice. In this situation, for low gas flow rates, the bubble volume remains essentially constant and the frequency of bubble production is proportional to the gas flow rate. This type of formation is referred to as constant-volume. For larger flow rates, the bubble frequency levels off to a constant value and the volume increases in proportion to the gas flow rate. This type of formation is referred to as constant-frequency. In our system, when $d < 2h$, we also observe a pseudo-constant-value regime where the bubble volume slightly increases as the frequency increases (Fig. 31. a, b and Fig. 34.). For $d > 2h$, the frequency slightly increases as the bubble volume increases (Fig. 36.).

We further investigated this transition by looking at the dynamics of the pinching phenomenon. Bubble formation results from the competition between viscous and capillary forces acting on the bubble. That is, capillary force depends on the surface of the generated interface, therefore it depends on the bubble length d . Using image processing, we measured the acceleration experienced by the generated bubbles during their detachment from the core bubble. For $d < 2h$, the bubble nucleation occurs in three different steps (see Fig. 37):

- (a) The core gas bubble is squeezed from the sides between the two liquid flows, inducing an acceleration of the bubble front.
- (b) When the bubble front crosses the mixing chamber, the bubble front expands to form an elongated bubble in the resulting channel. Meanwhile a neck is formed, inducing an increase of the total bubble surface area. The bubble deformation causes an increase of the capillary elastic restoring force that slows down the bubble front.
- (c) After the break-up, the generated bubble is ejected from the mother bubble. The bubble reaches its constant cruising velocity for about four times the channel width.

When $d > 2h$, the increase of surface during step b is negligible compared to the total surface, so the capillary restoring force is not large enough to compete with the drag force experienced by the bubble.

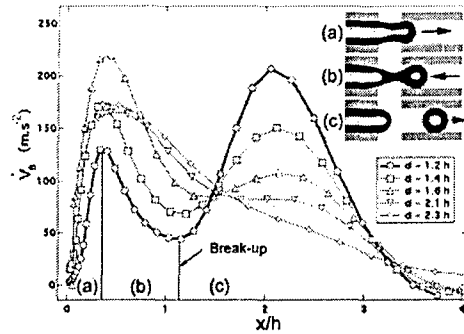


Figure 37: Acceleration experienced by the bubble front during bubble generation.

Pure liquid and gas flows

A. Flow phase diagram

The bubble generation system described above is used as an effective way to produce two-phase flows in microdevices. The channel width of the bubble generator is $50 \mu\text{m}$ and the different flow structures are observed in larger square channels ($200 \mu\text{m}$ or $525 \mu\text{m}$). Two-phase flows are distributed into several distinct flow patterns depending on the liquid and gas flow rates and fluid and channel properties. Five main flow regimes were observed in the partially wetting square microchannels: bubbly, wedging, slug, annular, and dry flows (see Fig. 38). Besides differences in definition of flow patterns, some typical regimes observed in larger channels such as stratified, churn or mist flows were not observed in our channels within the range of laminar flow rates investigated.

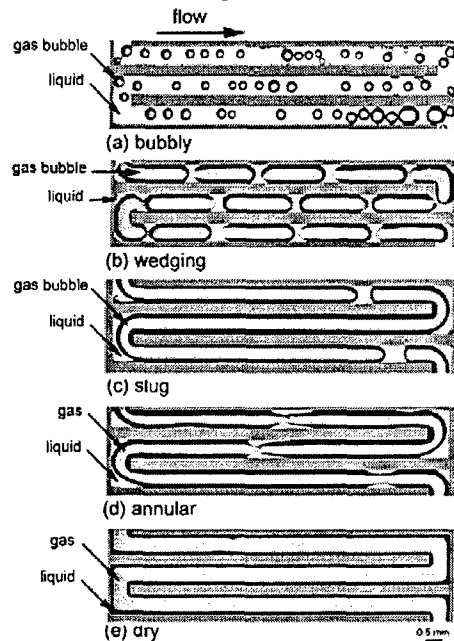


Figure 38: Flow patterns from high to low liquid fraction α_L .

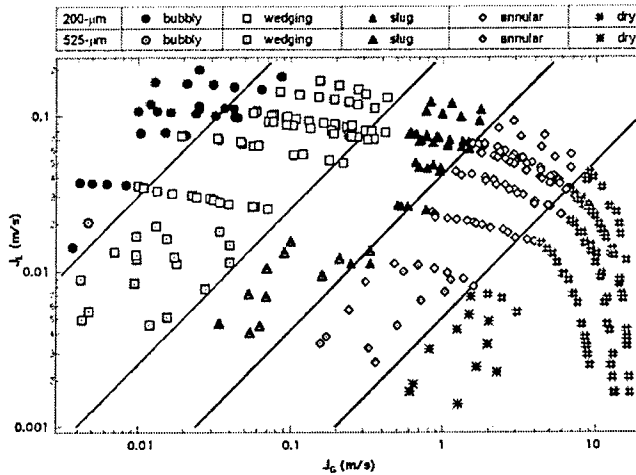


Figure 39: Flow pattern map for horizontal flow in 200- and 525- μm square channels, air-water.

Figure 39 shows the flow map and the transition lines between flow regimes for 200- and 525- μm channels. Liquid superficial velocity ($J_L = Q_L/A$, where A is the cross section area) is plotted against gas superficial velocity ($J_G = Q_G/A$). Each set of experiments is conducted maintaining a constant liquid inlet pressure while gradually increasing the gas inlet pressure. The liquid flow rate Q_L then decreases because of the increase of the hydraulic resistance of the channel. Flow regime transitions are determined by visualization and examination of pressure drop data. Transitions between regimes are predictable as a function of liquid and gas flow rates. For both 200- and 525- μm channels, transitions between each regime occur for fixed values of the homogeneous liquid fraction α_L defined as:

$$\alpha_L = \frac{Q_L}{Q_L + Q_G} \quad (2)$$

The bubbly/wedging transition is for $\alpha_L \approx 0.75$; the wedging/slug transition is for $\alpha_L \approx 0.20$; the slug/annular transition is for $\alpha_L \approx 0.04$; and the annular/dry transition is for $\alpha_L \approx 0.005$, as can be seen Fig. 39. While other transitions are smooth, the wedging/slug transition presents some hysteresis if the gas flow rate is increased or decreased. For $\alpha_L \approx 0.20 \pm 0.01$, the system is metastable, switching from a state to another at the same liquid and gas inlet pressure.

Over the range of flow rates investigated, because surface tension is predominant, transitions in square microchannels are not dependent on the channel diameter. This case is different from the case of macro and mini channels (when $h > 1 \text{ mm}$) where differences in the relative effects of gravitational, shear, and surface tension forces cause the transitions to be dependent on the channel diameter.²² For a square channel, the hydraulic diameter is equal to the channel width h . Experiments in triangular microchannels pointed out the relevance of sharp edges in flow regime transitions.

B. Bubble velocity

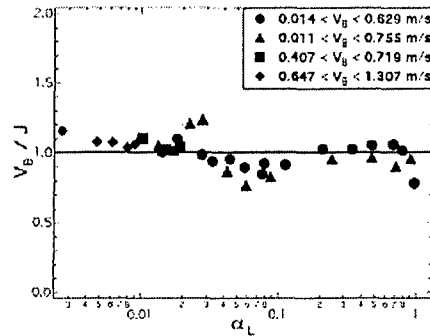


Figure: 40: Comparison of the bubble velocity V_B (measured by image processing) with the average superficial velocity J (measured with liquid and the gas flow meters) as a function of the homogeneous liquid fraction α_L for different initial conditions ($h = 525 \mu\text{m}$).

For bubbly, wedging and slug flows, the bubble velocity V_B is measured from processing consecutive images taken with a high-speed camera at 10,000 frames per second. For annular and dry flows the term “bubble” cannot be defined nor can the velocity be optically measured. For different homogeneous liquid fractions α_L , Fig. 40 compares the measured bubble velocity V_B to the average superficial velocity J , defined as the sum of the liquid and the gas superficial velocities:

$$V_B \approx J_L + J_G = J \quad (3)$$

Over the range of measured velocities (from 0.01 to 1 m/s), the bubble velocity V_B can be assimilated to the average superficial velocity J . This result suggests that there is no corner flow. Contrary to circular channels, no characteristic drift-velocity between bubbles and the average speed of the fluid was measured in the present investigation. In studies using circular channels, as the channel diameter shrinks, drift-velocity is reduced²¹ and removed under microgravity conditions due to lack of buoyancy between liquid and gas.²⁵

C. Apparent versus homogeneous void fraction

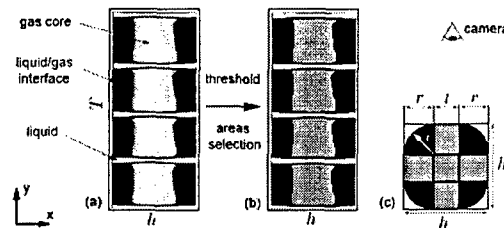


Figure 41: Image processing to calculate the apparent void fraction ϵ_G , (a) Part of a raw time-space diagram (wedging flow), (b) threshold and area identified time-space diagram, (c) characteristic symmetries of a channel cross-section.

From image processing, the apparent time-averaged void fraction ϵ_G is calculated. Time-space diagrams are created from movies with a line plotted normal to the channel. For each liquid and gas flow rate, a composite image is created where the x coordinate

corresponds to the channel width h and the y coordinate corresponds to the time t (Fig. 41 (left)). As the liquid air interface possesses symmetries with respect to the center axis of the channel (Fig. 41 (right)), ϵ_G is calculated as follow:

$$\epsilon_G = \frac{\frac{\pi}{4} \sum d_i^2 + \sum (2l_i h - l_i^2)}{Th^2} \quad (4)$$

where $d_i = 2r$ is the diameter of the curved interface, h is the height (and width) of the channel, l_i is the width of the core gas in "contact" with the walls, and $T = \sum t$ corresponds to the time of acquisition. Except for the bubbly flow (where $l_i = 0$), the liquid film between the gas and the center of the walls is neglected in the calculation of the total liquid volume because it is negligible compared the liquid volume in the corners. The apparent liquid fraction ϵ_L is simply defined as:

$$\epsilon_L = 1 - \epsilon_G \quad (5)$$

Figure 42 shows the relation between the apparent liquid fraction ϵ_L and the homogeneous liquid fraction α_L . Transitions between flow regimes are shown by straight vertical lines. Deviation from a linear relationship between ϵ_L and α_L occurs from the slug flow for $\epsilon_L < 0.02$. Kolb and Cerro showed the transition from an axisymmetrical to a symmetrical semi-infinite bubble profile in square channels when the capillary number Ca increases. This behavior results in an increase of the liquid fraction with the gas flow rate. The fact that the apparent void fraction ϵ_L does not increase monotonically with Ca is specific to polygonal channels.

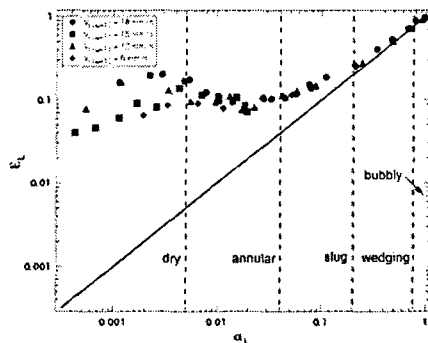


Figure 42: Apparent liquid fraction ϵ_L vs homogeneous liquid fraction α_L for different initial conditions ($h = 525 \mu\text{m}$).

From the calculation of the apparent liquid and void fractions, the slip ratio S between liquid and gas can be defined as:

$$S = \frac{V_G}{V_L} = \frac{J_G \epsilon_L}{J_L \epsilon_G} \quad (6)$$

Figure 43 shows the slip ratio S as a function of the homogeneous liquid fraction α_L . For

the annular and the dry flow, experimental data suggests a relationship as:

$$S = 0.1\alpha_L^{-1} \quad (7)$$

The large slip between the two phases can be attributed to wall shear for the liquid, while the gas can flow unhindered in the channel core. S is meaningless for $\alpha_L = 0$. In a 100- μm circular channel, Kawahara et al reported a large slip ratio S compared to macro and mini channels. For example, they found $S \approx 16$ for $\alpha_L \approx 0.2$. In our case, the combined effect of noncircular capillaries and microsize channels dramatically enhances the slip ratio between liquid and gas.

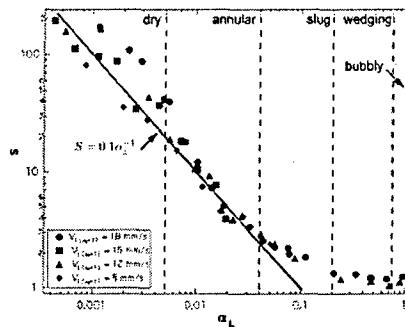


Figure 43: Slip ratio S between gas and liquid as a function of α_L for different initial conditions ($h = 525 \mu\text{m}$).

D. Flow patterns

D.1. Bubbly flow

In bubbly flow (Fig. 38 (a)), the gas phase is distributed as discrete spherical bubbles in a continuous liquid phase. The bubble size d is smaller than the channel height h . As individual bubbles may collide and coalesce to form large bubbles, polydispersity is observed. For low liquid velocities J_L , some bubbles adhere to the walls. The detachment of a bubble involves two forces, the drag force and the adhesion force. Experiments in slit microchannels related a critical bubble size to a critical capillary number for the bubble to detach for given receding and advancing contact angles. As the flow inside a square channel is non-axisymmetric close to the walls, and is modified by the presence of bubbles, different bubble sizes are trapped and released from the surface showing a random behavior. To observe the flow path around the bubbles, experiments were performed adding latex beads ($4 \mu\text{m}$) to the liquid. It has been found that bubbles pinned on the walls were actually spinning.

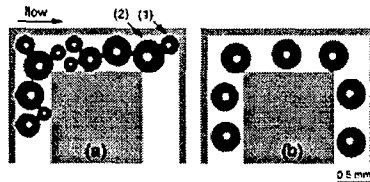


Figure 44: Bubbly flow: effect of a sharp return; (a) low liquid velocity, (b) high liquid velocity.

Specific to that flow regime, the bubble motion is dependent upon the channel orientation with respect to the gravity when $d \ll h$. The presented experiments were performed with horizontal channels. For low liquid velocity, bubble clogging occurs in sharp corner bends (Fig. 44 (a)). As the liquid flow in the vicinity of the corner is very small, a small bubble (1) can easily be trapped; the effective channel size is then reduced and a bubble too large to pass through the corner becomes trapped as well (2). Other bubbles become trapped as a chain reaction until they eventually merge and pass the bend. At higher liquid flow rates, bubbles are not perturbed by the sharp bend (Fig. 44 (b)). This effect can be removed using a curved bend. The bend effect on two-phase flow was investigated in larger channels and has been shown to increase coalescence of small bubbles in some flow conditions. In our experiments, bubble size and velocity were not significantly perturbed by this geometry except for the case discussed above. We note that the bubbly flow is not accessible to the system when a mechanical pump supplies the liquid.

D. 2. Wedging flow

The wedging flow (Fig. 38 (b)) consists of elongated bubbles, the size of which d is larger than the channel width h ($d > h$). When the flow is steadily developed ($\alpha_L < 0.70$), bubbles are equally spaced and monodisperse. The wedging flow exhibits some differences from the Taylor bubble flow, usually reported in the literature. For a partially wetting system, as a function of the bubble velocity V_B , bubbles can dry out the center of the channel creating triple lines (liquid/gas/solid). The liquid film between the gas and the center of the channel can be considered as static, while liquid flows in the corner. The film thickness δ was shown to depend on the bubble length d . A liquid film of thickness δ is known to be metastable if $\delta < \delta_C$, δ_C being the critical thickness defined by:

$$\delta_C = 2 \lambda_c \sin\left(\frac{\theta}{2}\right) \quad (8)$$

Where λ_C is the capillary length ($\lambda_C = (\bar{\alpha}g(\rho_L - \rho_G))^{1/2}$, where g is the gravity and ρ_L and ρ_G are respectively the liquid and gas densities). In that case, the film can dewet by nucleation and growth of dry patches when their size is greater than a critical value r_C defined as:

$$r_C = \frac{\delta}{l_r \sin \theta_r} \quad (9)$$

where l_r is a logarithmic function of r_C . For the capillary regime ($\lambda_C < r_C$), the dewetting velocity U_{dew} is constant and independent of the film thickness:

$$U_{dew} = \frac{U^* \theta^3}{6L_L} \quad (10)$$

Where U^* is the characteristic velocity of the liquid ($U^* = \lambda/\eta$) and L_L is a prefactor depending on the liquid. The dewetting velocity was measured from image processing on glass in the channel and was found to be $U_{dew} \approx 7$ mm/s. Three kinds of wedging bubbles were observed as a function of their velocity V_B (see Fig. 15):

(a) When $V_B < U_{dew}$, bubbles completely dry out the solid surface in the center of the channel. The contact angle at the front of the bubble is the receding contact angle θ_r and the one at the rear of the bubble is the advancing contact angle θ_a .

(b) When $U_{dew} < V_B < V_C$, bubbles present complex contact lines. The front of the bubble is lubricated because dry patches grow slower than the bubble speed. There is no contact angle at the front of the bubble. V_C is the critical bubble velocity for the center of the channel at rear of the bubble to be dried out ($V_C \approx U_{dew} d/h$). At the rear of the bubble, the contact angle is still the advancing contact angle θ_a .

(c) When $V_C < V_B$, bubbles are lubricated by a thin liquid film and there is no contact line.

Dry patches can start from the contact line close to the center of the walls but also directly from the film suggesting that heterogeneities can start the process. A few studies have been conducted on the shape of a dewetting contact line.

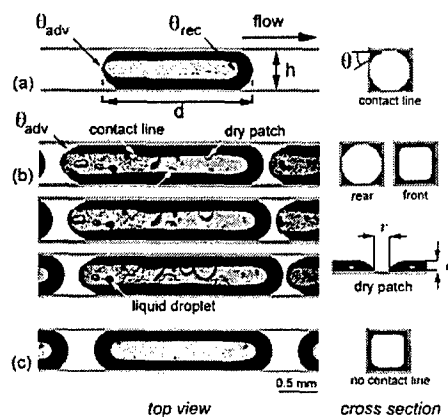


Figure 45: Wedging flow: (a) drying bubble, (b) consecutive images of a hybrid bubble, and (c) lubricated bubble.

D. 3. Slug flow

For $\alpha_L < 0.20$, bubbles distribute themselves in slug (Fig. 39 (c)). The bubble size is far larger than the channel height ($d \gg h$). Bubbles are surrounded by liquid so they do not touch the channel walls. For long bubbles the film between gas and solid may dry out. In a previous investigation, Wong *et al* demonstrated the decrease of the film thickness δ along the bubble. In some case, growing dry patches were locally observed at the bottom of the gas slug on specific channel locations, suggesting the nucleation was induced by local surface defects.

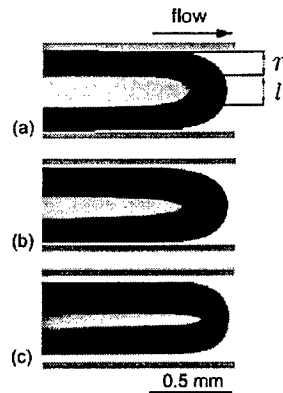


Figure 46: Slug flow: bubble noses for different capillary numbers; (a) $Ca \approx 0.009$, (b) $Ca \approx 0.013$, and (c) $Ca \approx 0.018$.

The nose of the bubbles has a characteristic bullet-shape. When a semi-infinite bubble is injected into a liquid filled square capillary, Kolb and Cerro studied the transition from a non-axisymmetric bubble nose profile to an axisymmetric bubble nose profile for a capillary number of $Ca \approx 0.1$. In the case of a bubble-train flow, when liquid is coflowing with gas, Fig. 46 represents the bubble nose profile for different Ca . The radius of curvature of the liquid/gas interface increases while the size of the core gas diminishes, suggesting a transition from a non-axisymmetric profile to an axisymmetric profile for a lower Ca . In our experiments, within the range of the liquid and gas flow rates investigated, $Ca \approx 0.1$ corresponds to an annular or to a dry flow. The change of the bubble profile affects the apparent liquid fraction ε_L . The apparent liquid fraction does not decrease monotonically with the gas flow rate in our pressurized system. An interesting feature of the slug flow is the recirculating liquid flow between bubbles, leading to different degrees of mixing, as a function of Ca .

D. 4. Annular flow

As the liquid fraction α_L decreases, the size of the bubbles increases until the bubble size is equal to the channel length ($d = L$); the flow becomes then annular (see Fig. 39 (d)). In that situation, a continuous central gas core is surrounded by liquid. As in larger channels, interfacial waves along the gas core were observed. This flow regime is known to be rather complex because of transient phenomena depending on the nature of the waves (ripples, flooding and disturbance waves). In square microchannels, because of the importance of capillary effects, no droplets entrainment i.e. mist flow was observed over the range of flow rates investigated. Waves are composed of liquid rings traveling along the gas core. Fig. 47 shows an example of complex wave propagation. A time-space diagram was created along part of the channel; pictures (a), (b) and (c) represent different times as indicated on the diagram. The waves oscillate, they can go upstream and their random motion does not suggest any correlation between them (wave (2) is moving away from wave (1)). Liquid rings can grow and disappear from the flow inside the channel. As in triangular geometry, as α_L decreases, pressure fluctuations decrease. However, the mean pressure inside the channel is constant for given liquid and gas flow rates. The wave velocity is largely slower than the gas motion. As a gas cylinder is highly unstable

compared to a liquid cylinder, further work is required to understand those phenomena.

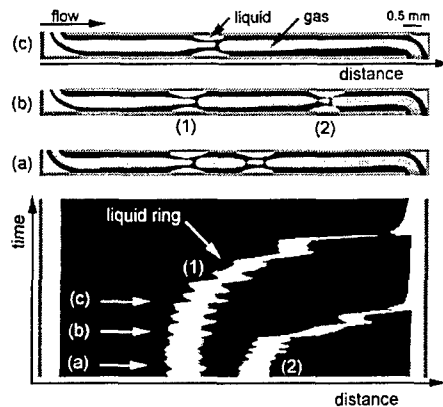


Figure 47: Annular flow: time-space diagram of liquid ring motion along the gas core.

D. 5. Dry flow

When $\alpha_G > 0.995$, the gas core becomes more and more steady. Waves disappear and the liquid is only transported on the wedges. The liquid film thickness decreases until the stability limit is reached so dry patches can grow. When the film dries out, as a result of dewetting processes, liquid droplets stay on the solid wall (see Fig. 48). The radial size of the gas/solid contact l increases with the gas flow rate Q_G , as α_L decreases. Single gas flow occurs when $l = h$.

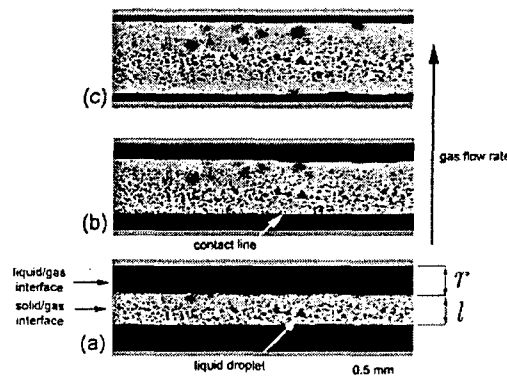


Figure 48: Dry flow: the central gas core dries out the center of channel walls.

E. Pressure drop

Pressure drop caused by frictional force in two-phase flow is a parameter of prime interest to determine the conditions for the flow. A typical plot of the pressure drop as a function of the capillary number $Ca = \eta_L J / \gamma$ is shown in Fig. 49. Each flow regime has a different dependence on Ca , except for the bubbly and the wedging flow. On the other hand, when ΔP is plotted versus the gas superficial velocity (Fig. 49 (right)), the transition between bubbly and wedging flows appears clearly. The transition from the

wedging to the slug flow causes a large drop in pressure. At the same gas inlet and liquid inlet pressure, the system switches from one regime to another. The slug flow presents an interesting feature of decay of pressure with gas flow rate. Ratulowski *et al* proposed an expression for the pressure, assuming that the pressure drop is the sum of the pressure across bubbles and liquid slugs. They found an expression for the pressure that is proportional to the number of bubbles in the channel nb . As nb is decreasing with the gas flow rate for a given channel of length L , the pressure drop decreases for the slug flow. For the annular flow, the presence of a maximum in the pressure gradient was observed in larger channels, and it was attributed to a transition from a mist flow to an annular flow. In our case, as the liquid volume fraction α_L decreases, the liquid friction decreases as well. For the dry flow, the effective channel size for the gas flow approaches that of single gas flow and the pressure converges asymptotically to the single gas one.

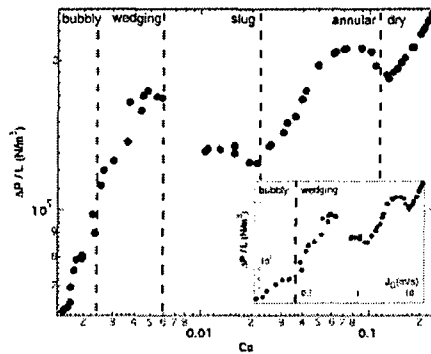


Figure 49: Typical pressure drop measurement ΔP as a function of the capillary number Ca ($h = 200 \mu\text{m}$). Transitions between flow regimes cause a change on the pressure drop dependence on Ca and J_G .

E.1. Single-phase flow

For a laminar steady state flow of fluid i in a square channel ($Re < 3000$), the pressure gradient is related to the flow rate as:

$$Q_i = \frac{h^4}{A \eta_i} \nabla P \quad (12)$$

where $A \approx 28.43$ is a numerical constant, h is the channel height, and η_i is the dynamic viscosity of fluid i . Analogous to electrical resistance, fluidic resistance R is defined as the ratio of pressure difference over flow rate. Assuming a constant pressure gradient along the channel of length L and using Eq. (12), fluidic resistance R_i of fluid i can be written as:

$$R = A \frac{L \eta_i}{h^4} \quad (13)$$

For the 200- and the 525- μm square channels, the DI water resistance R_L was calculated

from 0.01 to 0.5 cm³/mn, and the air resistance R_G was calculated from 0.01 to 30 cm³/mn. From pressure measurements, in the 200- μ m channels, $R_{L(\text{exp})} / L \approx 1.64 \times 10^{13}$ kg·m⁻⁵·s⁻¹ and $R_{G(\text{exp})} / L \approx 3.19 \times 10^{11}$ kg·m⁻⁵·s⁻¹. Using Eq. (13) with the uncertainties on the channel sizes, $\Delta h = 10 \mu\text{m}$, the calculated resistance values, $R_{L(\text{theo})} / L = 1.78 \pm 0.40 \times 10^{13}$ kg·m⁻⁵·s⁻¹ and $R_{G(\text{theo})} / L = 3.23 \pm 0.74 \times 10^{11}$ kg·m⁻⁵·s⁻¹, agree well with the measured resistances per unit of length. As well, in the 525- μ m channels, experimental resistances, $R_{L(\text{exp})} / L \approx 3.56 \times 10^{11}$ kg·m⁻⁵·s⁻¹ and $R_{G(\text{exp})} / L \approx 6.55 \times 10^{11}$ kg·m⁻⁵·s⁻¹, are consistent with the resistances calculated using Eq. (12), $R_{L(\text{theo})} / L = 3.74 \pm 0.30 \times 10^{13}$ kg·m⁻⁵·s⁻¹ and $R_{G(\text{theo})} / L = 6.81 \pm 0.54 \times 10^{11}$ kg·m⁻⁵·s⁻¹.

E. 2. Two-phase flow

Two-phase flow pressure drop is greater than that of single-phase flow. Different models have been proposed to predict the pressure drop across a bubble train in square capillary. Ransohoff *et al* proposed a dimensionless flow resistance $\beta = h^2 \text{grad } P / \eta J$. Ratulowski *et al* correlated the pressure drop to the capillary number: $\Delta P = a \text{Ca}^n$, where a and n are numerical constants depending on the bubble shape (axisymmetric or nonaxisymmetric). Wong *et al* took into account the capillary geometry and the bubble length for the pressure-velocity calculation for bubble flow in polygonal capillaries. They found that pressure drop scales linearly with Ca when the liquid bypasses the bubble through corner channels (corner flow) and that it scales with $\text{Ca}^{2/3}$ when the liquid is essentially pushing the bubble (plug flow). Stanley *et al* analyzed their pressure drop data in different square microchannels using the homogeneous flow model with the Fanning equation leading to $f = C/\text{Re}^n$, where f is the friction coefficient, C and n are numerical constants depending on the flow (laminar or turbulent), and Re is the Reynolds number.

Applied to our experimental data these correlations were inaccurate in predicting the measured pressure drops ΔP . This can be attributed to several factors. First, the dependence of the slip ratio S between liquid and gas velocities on the homogeneous liquid fraction α_L (Eq. (7)) hinders the use of an apparent viscosity of the mixture used to calculate the capillary number Ca and the Reynolds number Re . Also, the change in pressure ΔP that is dependent on the average mixture velocity J between the annular and dry flows disables a model that takes into account a monotonical change of the slip ratio S with J . The Lockhart and Martinelli model did not provide good prediction nor transition between flow patterns. This is not surprising as Lockhart-Martinelli correlations are known to provide poor agreement when the flow is laminar.

Since liquid is mostly flowing along the channel walls, the contribution of the liquid viscosity to the frictional pressure drop is predominant. Figure 20 shows the evolution of the pressure drop for 200- μ m square channels as a function of the homogeneous liquid fraction α_L . The two-phase pressure drop $\Delta P_{2\text{-phase}}$ was scaled by the single liquid flow pressure drop ΔP_L associated to the liquid flow rate Q_L in the channel ($\Delta P_L = R_L Q_L$). As can be seen in the figure, data collapse more or less on a single master curve with two distinct regimes. The bubbly and the wedging flows are depicted on one side and the slug, annular and dry flows are on the other side. For the bubbly and the wedging flow, the pressure drop associated can be written:

$$\Delta P_{2\text{-phase}} = \Delta P_L \alpha_L^{-1}$$

(14)

In that case the flow can simply be considered as a single liquid flow with a velocity V corresponding to the mean liquid velocity $V_L = J_L/\alpha_L$. As can be seen in Fig. 50, the deviation to Eq. (14) increases as the liquid velocity decreases (circles and squares) because of wetting phenomena (see wedging flow).

For smaller liquid fraction, the homogeneous model is not realistic because of the slip between the phases. Nevertheless, a simple empirical correlation for the pressure can be written as:

$$\Delta P_{2\text{-phase}} = \Delta P_L \alpha_L^{-1/2} \quad (15)$$

This equation better fits the data for high liquid flow rate.

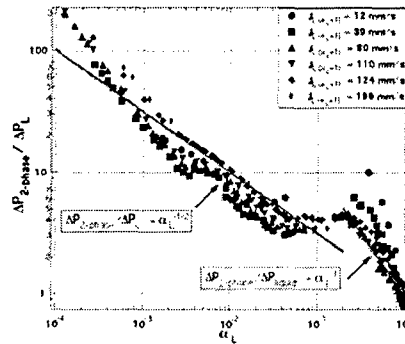


Figure 50: Two-phase flow pressure drop scaled by single liquid flow pressure drop as a function of homogeneous liquid volume fraction α_L ($h = 200 \mu\text{m}$).

As α_L changes from 1 to 0, the system goes from a single liquid flow to a single gas flow. The fluidic resistance $R = \Delta P/Q$ is an interesting parameter because it is calculable from direct measurements without assuming any correlation. The two-phase flow fluidic resistance $R_{2\text{-phase}}$ can be defined as:

$$R_{2\text{-phase}} = \frac{\Delta P_{2\text{-phase}}}{Q_L + Q_G} \quad (16)$$

Figure 51 shows the variation of $R_{2\text{-phase}}$ with the homogeneous liquid fraction α_L . For high liquid fractions, using Eq. (14), $R_{2\text{-phase}}$ can be written:

$$R_{2\text{-phase}} = R_L \quad (17)$$

The deviation for slow liquid velocity appears clearly as contact lines increase the resistance to flow. For low liquid fractions, using Eq. (15) $R_{2\text{-phase}}$, can be written as:

$$R_{2\text{-phase}} = R_L \alpha_L^{1/2} \quad (18)$$

At the transition between the annular and the dry flow, the flow can be seen as a gas flow in a circular tube of diameter h and a liquid flow in the corners. The gas resistance in a circular tube of diameter h is $R_{G, \text{circular}} = 128 \eta_G L / \pi h^4$. In this situation, assuming that the contribution to the pressure drop is essentially due to the gas flow because of the large slip ratio, the two-phase resistance can be written $R_{2\text{-phase}} \approx R_{G, \text{circular}} \approx 0.026 R_L$ for the case of water and air. As can be seen Fig. 47, the two-phase flow resistance $R_{2\text{-phase}}$ experimentally converges to the calculated circular channel gas resistance $R_{G, \text{circular}}$ for $\alpha_L < 10^{-3}$.

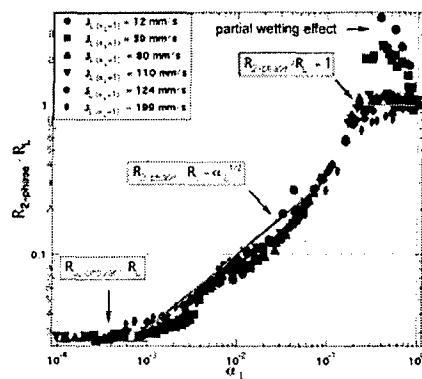


Figure 51: Two-phase fluidic resistance $R_{2\text{-phase}}$ compared to liquid resistance R_L as a function of homogeneous liquid fraction α_L ($h = 200 \mu\text{m}$).

Liquid with surface active agent and gas flow in microchannels

A. Flow phase diagram and flow patterns

We investigated the effect of impurities added to the liquid on multiphase flow. When surface active agent (SDS) is added to the liquid, foam flow is observed (Fig 52 and Fig 53). The addition of SDS molecules to water essentially prevents bubble coalescence. Wet foam ($\alpha_L > 0.26$) is characterized by disordered distributions of spherical gas cells. To minimize surface energy, bubbles tend to remain spherical until they are too closely packed for $\alpha_L \approx 0.26$. This liquid fraction value represents the closest possible packing of monodisperse spherical objects corresponding to a face-centered cubic array. Dry foam ($0.02 < \alpha_L < 0.26$) is characterized by deformable polyhedral cells. As liquid fraction is lowered, cell shape departs from a sphere as bubble surfaces commence to flatten along cell boundaries forming planar films at the intersection of two bubbles, Plateau borders at the intersection of three bubbles, and vertex at the intersection of four bubbles. The dry foam is formed of a network of thin liquid films and menisci, the stability of which depends on the relative effect of shear. Ordered (monodisperse) polyhedral flow as well as disordered (polydisperse) polyhedral flows are observed as a function liquid and gas flow rates. For specific conditions, ordered arrays of bubbles are formed with different number of rows N per channel width as a function of bubble size, liquid fraction, and shear. Higher shear induces bubble coalescence by film rupture. Bubble coalescence induces a spatial reorganization of the foam. Foam evolves with avalanche dynamics where an event triggers a local chain-reaction of cell spatial reorganization.

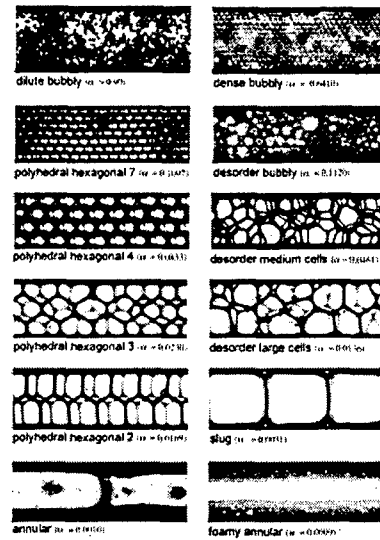


Figure 52: Foam flow patterns in square microchannel ($w = 525$ microns) for various liquid fractions.

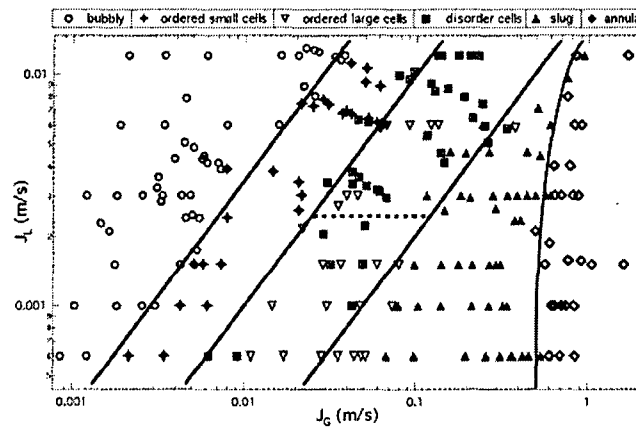


Figure 53: Aqueous foam phase diagram in 525 um square channel with 50 microns mixer (water and SDS at 8 mM/L, and air)

B. Effective viscosity

Probably one of the most striking properties of foams is their huge hydraulic resistance. The rheological properties of the mixture are dramatically affected by the liquid fraction. Different model have been proposed to describe the rheological properties of foam. Foam is usually assumed to be a pseudo-plastic liquid. Theory suggests that very wet foams, the effective viscosity should follow the Einstein relation:

$$\eta_{eff} = \eta_L (1 + 2.5\alpha_G) \quad (19)$$

Where $\alpha_G = 1 - \alpha_L$, is the gas volumetric fraction also called void fraction or foam quality. We measured the pressure drop ΔP_{eff} of aqueous foam flow in serpentine square

microchannels for various liquid and gas flow rates. An effective shear viscosity can be associated to the produced aqueous foam. Assuming a laminar flow, the effective foam fluidic resistance R_{eff} can be measured as the ratio of pressure difference ΔP_{eff} over flow rate $Q_{\text{eff}} = Q_L + Q_G$. For a square duct, the fluidic resistance of fluid i is $R_i = AL\eta_i/w^4$ where $A \sim 28.43$ is a numerical constant, L is the channel length and η_i is the dynamic viscosity of fluid i . Therefore one can write

$$\frac{R_{\text{eff}}}{R_L} = \frac{\eta_{\text{eff}}}{\eta_L} \quad (20)$$

Fig. 24. displays the effective viscosity of the foam normalized by the liquid viscosity as a function of the liquid fraction for different flow rates. For comparison to the non-surfactant case, we plotted on the figure the scaled effective viscosity of a pure DI water and air flow prepared the same way (50 microns mixer, 525 square channel). Data collected for four different initial conditions collapse more or less in a single master curve for $\alpha_L > 0.02$ and shear thinning behavior is observed for $\alpha_L < 0.02$. Data for $\alpha_L > 0.02$, suggests that the system dissipates the same amount of energy relatively independently of the order parameter of the foam. The effective foam viscosity is several orders of magnitude higher than the liquid viscosity. The transition at $\alpha_L \sim 0.02$, correspond to the multi-cells/slug flow transition. For $0.05 < \alpha_L < 1$, experimental data suggests a scaling such as:

$$\eta_{\text{eff}} = \eta_L \alpha_L^{-2.5} \quad (21)$$

It is worth noting that eq. 21. can be expressed in terms of void fraction $\alpha_G = 1 - \alpha_L$. Therefore, for a very dilute wet foam ($\alpha_G \ll 1$), Eq. 21. reduces to the Einstein formula (Eq. 19.). The experimental scaling law can be interpreted as an extension of the Einstein relationship to a much larger range of validity ($0.05 < \alpha_L < 1$). It is particularly interesting to consider that even if bubbles interact and deform way beyond a spherical shape, the system unexpectedly exhibits an effective viscosity of a suspension of rigid spheres.

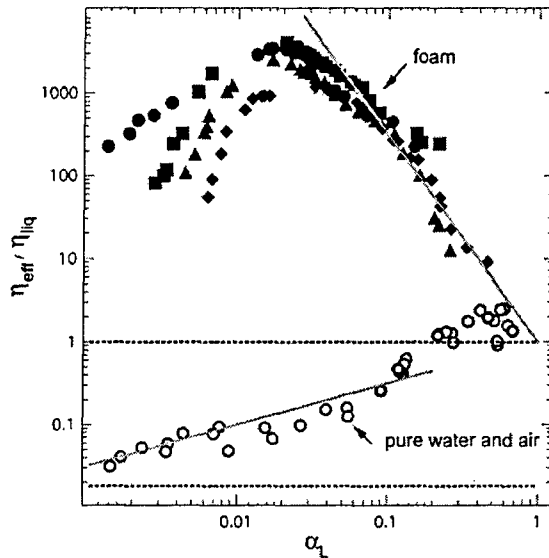


Figure 54: Liquid/gas mixture effective viscosity vs liquid fraction

Effect of hydrophobic walls on flow patterns

A. Pure liquid gas flow

Previous investigations were performed in hydrophilic channels with a low contact angle ($9^\circ < \theta < 25^\circ$). In the following section, channels were coated with Teflon[®] producing a static contact angle $\theta \approx 120^\circ$ for pure water and air. Liquid/gas flows in hydrophobic channels are very different than the ones observed in hydrophilic channels. In hydrophobic channels, bubbles are not lubricated and their motion is subject to contact line friction at the channel walls. Contact angle hysteresis can be seen in Fig. 55 (a) and (b). In these figures, the advancing contact angle $\theta_{\text{adv}} > \pi/2$, the receding contact angle $\theta_{\text{rec}} < \pi/2$, and the interface curvature follows the flow direction. Small bubbles are trapped in the sharp channel corners. Although the hydrophobic flow is quite unsteady, three distinct flow patterns were identified for different void fractions as shown in Fig. 25:

- (a) Isolated asymmetric bubble flow is observed in the case of low void fractions, since the surface energy is low, small bubbles adhere to the channel walls. After many bubbles merge together, a large gas plug occupying the entire channel cross-section is formed and is pushed by the liquid flow.
- (b) For intermediate void fractions, the flow is composed of liquid and gas plugs. Bubbles and droplets are not symmetric in the direction of the flow. Interface instabilities cause asymmetry with respect to the channel axis. A corner can block a bubble until another bubble joins it and forms a bigger one, as shown on the lower channel in Fig. 55.b.
- (c) For high void fractions, the flow consists of small liquid droplets adhering to the channel wall, while gas is flowing in the center of the channel. Droplets move randomly. When droplets merge to form a droplet larger than the channel size, the resulting liquid plug is advected by gas flow. This liquid plug collects small liquid droplets on its path.

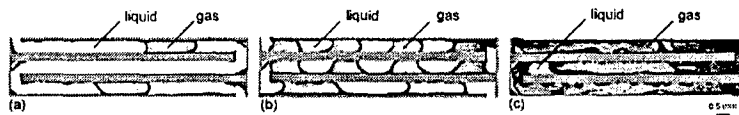


Figure 55: Pure water/air flow patterns in hydrophobic channels. From low to high void fractions. (a) isolated asymmetric bubble flow, (b) wavy bubble flow, (c) scattered droplet flow.

B. Foam flow

For the case of liquid/gas flows with surfactant in hydrophobic channels, we have identified two principal flow regimes that are a combination of previously described flow patterns: bubbly-droplet flow for high void fractions (Fig. 56. a), and bubbly-plug flow for low void fractions (Fig. 56. b):

(a) For the bubbly-droplet flow, moving liquid droplets are stuffed with small gas bubbles. Changing the liquid and gas flow rates induces a change in size and distance between droplets. These droplets are created by collecting multiple droplets where small gas bubbles were trapped.

(b) The bubbly-plug flow is a combination of bubbly and plug flows. The gas plug is moving at the same velocity as the liquid. Consequently, the gas plug pushes small bubbles downstream. As for the bubbly-droplet flow, size and distance between plugs is adjustable by changing the liquid and gas flow rates. For very low void fractions, the flow is bubbly and is frequently perturbed by large plugs pushing all the small bubbles downstream.

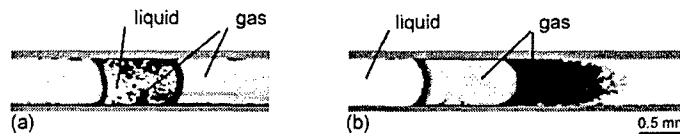


Figure 56: Water with surfactant/air flow patterns in hydrophobic channels. From high to low void fractions. (a) bubbly-droplet flow, (b) bubbly-plug flow.

Numerical Study of Bubble Transport in Microchannels

The objective of the numerical study was to develop a simulation tool for studying two-phase flow in micro fuel cells. The algorithm for the numerical simulation code was based on a level-set method based scheme for two-phase flows. The governing equations are discretized on a standard MAC grid. The velocities are defined at the appropriate cell walls, the pressure, density, and level set function are defined at the cell center. The convective terms are discretized using a 5th order WENO scheme and the time advancement is carried out using a 3rd order Runge-Kutta method. The poisson equation for pressure is solved using a multigrid Gauss-Seidel iterative method.

The numerical simulation tool was used to simulate the micro bubble generation process (described above in the experimental section). A schematic of the numerical computation domain is shown in Fig. 57. The initial focus was on completing a grid independence

study for the numerical simulations used to study a cross-shaped gas/liquid mixing section which produces gas bubbles co-flowing with liquids in a micro-channel. The grid independence study involves solving the same test cases using different grid sizes to ensure that the numerical results are indeed converging and are independent of the size or number of grid points used in the simulation. In the numerical simulations the liquid and

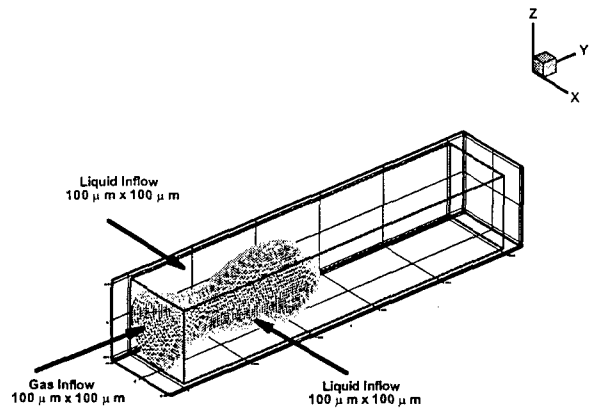


Figure 57: Schematic of numerical simulations for studying the bubble pinching process.

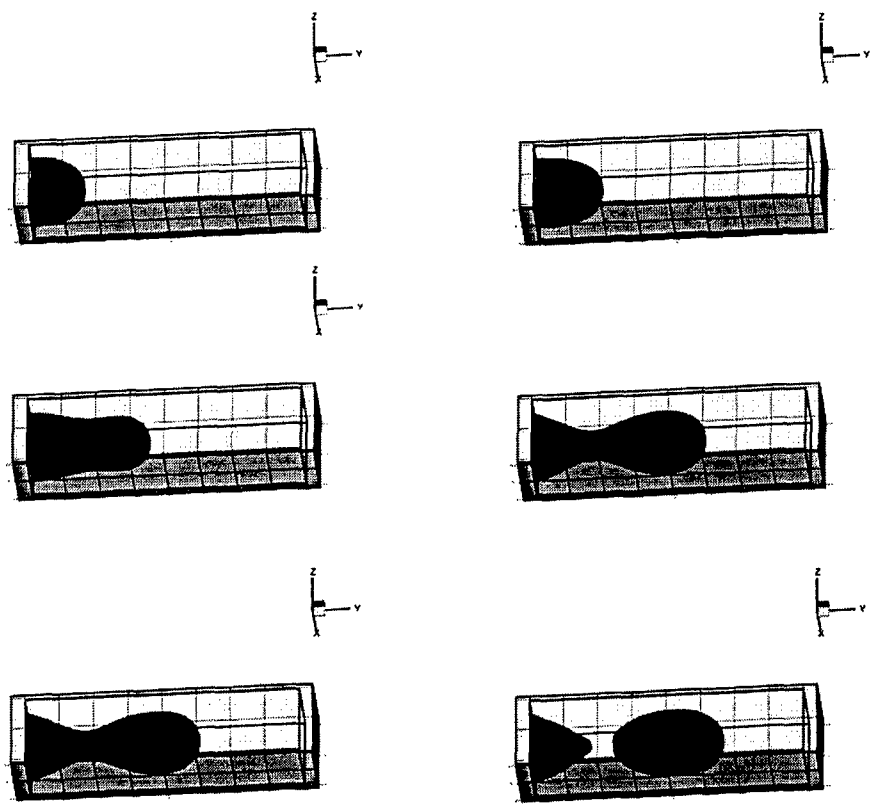


Figure 58: Sequence of plots showing the bubble pinching process for the $\alpha_L=0.67$ case.

gas flow rates were varied and their effects on the bubble sizes and frequencies were studied. Figure 58 shows the pinching process through a sequence of plots which show the liquid/gas interface at various instants in time. The elongation of the interface and the subsequent pinching due to the liquid cross-flow can be clearly seen. The simulations were conducted for homogeneous liquid fractions of 0.5, 0.67, and 0.8. The comparison of bubble sizes from the numerical simulations with experimental and theoretical results is shown in Fig. 59. The bubble size variation with the liquid fraction is plotted in the figure. The results show good agreement of the numerical results with the experimental and theoretical results. In addition, the grid independence study was also completed. In Fig. 59 the cases for homogeneous liquid fractions of 0.5 and 0.67 were computed using three different grid sizes. As seen from the results, the bubble sizes computed are grid independent.

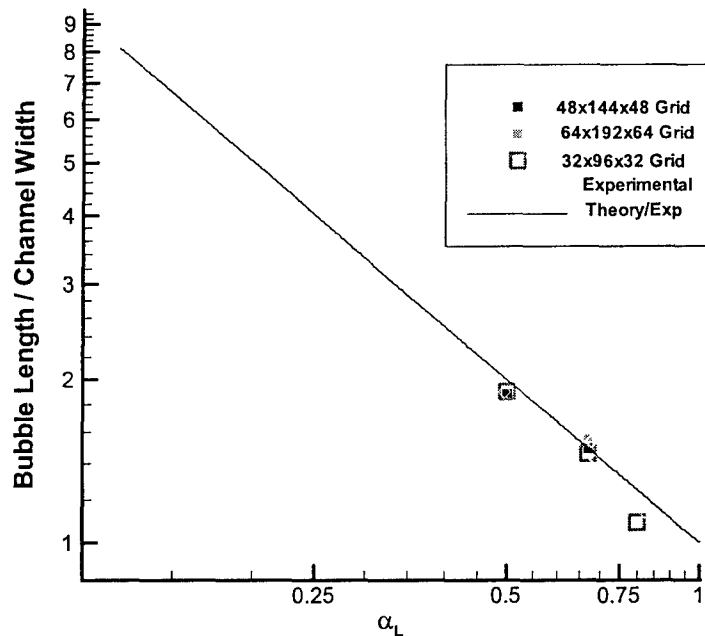


Figure 59: Comparison of numerical results with experimental data and theory for variation of bubble sizes with the channel size, liquid and gas flow rates.

In addition, 2-D simulation studies were conducted for grid independence studies and to study the effects of surface tension variations. The results were found to be grid independent. In addition to the level-set based method, a 1-D and 2-D simulation tool for studying the feasibility of a diffusion process based fuel cell was also developed.

Conclusions

In the project we made significant progress in our research towards reaching the final goal of developing self-activated micro direct methanol fuel cells. We have proved the concept and developed various tools for such development. Some of the research successes of the project are outlined below.

- A Si-based μ DMFC was developed and its electrochemical characteristics studied. Peak power density reached 50 mW/cm² at 60°C.
- A new MEA design was successfully developed to mitigate MeOH crossover without requiring novel membranes.
- Much improved performance of μ DMFC was achieved by using photochemically etched stainless steel bipolar plates. The maximum power density reached 100 mW/cm² at 60°C and atmospheric pressure.
- Flow visualization in the transparent DMFC indicated that efficient removal of carbon dioxide bubbles from the anode is important for cell performance.
- Water crossover through the membrane was found to be a critical issue to limit direct use of high concentration fuel, for the first time. A solution using the capillary pressure to push water back from the cathode to anode and a thin membrane such as Nafion 112 has been successfully developed. The net water crossover through the membrane was reduced by a factor of five. This paves the way to directly use concentrated fuel on the anode.
- An 8-cell air-breathing DMFC stack was developed and demonstrated. Cathode flooding was totally avoided using our newly developed water management strategy. It was found that O₂ transport in air-breathing operation is sufficient.
- Most recently, preliminary results demonstrated that it is feasible to finally use pure methanol in a completely passive DMFC.
- Liquid/gas multiphase flows in square microchannels present a large variety of flow patterns that are strongly correlated to specific channel geometries and properties of the liquid/gas, liquid/solid, and solid/gas interfaces. We presented an overview of multiphase flow in microchannel geometries. We investigated the shape of static elongated bubbles in square channels for different contact angles
- We investigated the bubble generation process in well-defined micro-geometry and found a simple scaling law for the bubble size as a function of operating parameter. This production technique was utilized to investigate multiphase flow in microchannels with surface modification.

- The wettability (hydrophilic/hydrophobic) as well as the presence of impurities in the fuel dramatically influence the operating conditions of the device. We proposed empirical correlations for the effective viscosity of a mixture of gas and either pure liquid or either liquid with impurities. The effective viscosity allows for the prediction of the energy requirement to drive fuel in the μ DMFC.
- Developed a numerical simulation tool for studying multiphase flows in micro devices. Numerical simulations were used to study bubble transport in micro channels and were found to be in good agreement with experimental results.

Publications

The following are papers and publications based on the work in the project:

1. C.Y. Wang, "Fundamental models for fuel cell engineering" Chemical Reviews, Vol. 104, pp.4727-4766, 2004.
2. C. Y. Wang, "Two-Phase Flow and Transport" Handbook of Fuel Cells - Fundamentals, Technology and Applications, Vol. 3, Part 3, pp.337-347,2003.
3. G.Q.Lu and C-Y Wang, Two-phase microfluidics, heat and mass transport in direct methanol fuel cells, an invited review chapter for New Developments in Heat Transfer, Editor by B. Sunden and M. Fahgri. WIT Press. In press. 2005.
4. G.Q. Lu, P.C. Lim, F.Q. Liu and C.Y. Wang "On mass transport in air-breathing DMFC stack" International Journal of Energy Research, in press.
5. G.Q. Lu and C.Y. Wang "Development of Micro Direct Methanol Fuel Cells for High Power Applications" Journal of Power Sources, Vol. 144, pp. 141-145, 2005.
6. G. Q. Lu, F. Q. Liu and C. Y. Wang, Water Transport Through Nafion 112 Membrane in Direct Methanol Fuel Cells. Electrochemical and Solid-State Letters, 8(1) A1-A4, 2005.
7. G. Q. Lu, C. Y. Wang, T .J. Yen and X. Zhang, Development and characterization of a silicon-based micro direct methanol fuel cell, Electrochimica Acta. 49 (2004) 821–828
8. G. Q. Lu and C. Y. Wang, Electrochemical and flow characterization of a direct methanol fuel cell, Journal of Power Sources, 134 (2004), 33-40.
9. T. J. Yen, N. Fang, X. Zhang, G. Q. Lu and C. Y. Wang, A micro methanol fuel cell operating at near room temperature, Applied Physics Letters, V.83, n.19, (2003) 4056-4058.
10. F.Q. Liu and C.Y. Wang, "Variations in interfacial properties during cell conditioning and influence of heat-treatment of ionomer on characteristics of direct methanol fuel cells" Electrochimica Acta, Vol. 50, pp1413-1422, 2005.

11. C.Y. Wang, G.Q. Lu, F.Q. Liu, and Y. Pan, Development of stand-alone micro and portable direct methanol fuel cell systems, 205th Electrochemical Society Meeting, San Antonio, May 2004.
12. G. Q. Lu and C. Y. Wang, "Two-phase microfluidic visualization of direct methanol fuel cells", Electrochemical Society 204th Meeting, Orlando, FL, Nov. 2003.
13. G. Q. Lu and C. Y. Wang, Development of high performance micro DMFCs and DMFC stack, 3rd International conference of fuel cell science, Engineering and Technology, Ypsilanti, MI, 2005.
14. D.-S. Meng, J. Kim, and C.-J. Kim, "A Distributed Gas Breather for the Micro Direct Methanol Fuel Cell," Proc. The 16th IEEE Int. Conf. on Micro Electro Mechanical Systems, Kyoto, Japan, Jan., 2003, pp. 534-7.
15. D.-S. Meng, T. Cubaud, C.-M. Ho, and C.-J. Kim, "A Membrane Breather for Micro Fuel Cell with High Concentration Methanol," Tech. Dig. Solid State Sensor, Actuator and Microsystems Workshop, Hilton Head Island, SC, Jun., 2004, pp. 141-4.
16. D.-S. Meng and C.-J. C. Kim, "Self-aligned Micro Bubble Arrays by Using Surface Tension," 2004 ASME Int. Mechanical Engineering Congress and Exposition, Anaheim, CA, Nov., 2004, CD: IMECE 2004-62182.
17. D.-S. Meng and C.-J. Kim, "Micropumping by Directional Growth and Hydrophobic Venting of Bubbles," Proc. The 18th IEEE Int. Conf. on Micro Electro Mechanical Systems, Miami, FL, Jan., 2005, pp. 423-6.
18. D.-S. Meng, Y. Ju, and C.-J. Kim, "A Comparative Study of Electrolysis and Boiling for Bubble-Driven Microactuators," Tech. Dig. The 13th Int. Conf. on Solid-State Sensors, Actuators and Microsystems, Seoul, Korea, Jun., 2005.
19. T. Cubaud And C.-M Ho, "Transport of bubbles in square microchannels" *Phys. of Fluids*, 16, 4575 (2004)
20. T. Cubaud, U. Ulmanella, and C.-M. Ho, "Two-phase flow in microchannels with surface modifications" submitted to *Fluids. Dyn. Res.*
21. T. Cubaud, M. Tatineni, X. Zhong, and C.-M. Ho, "Bubble dispenser in microfluidic devices", submitted to *Phys. Rev. E*
22. T. Cubaud and C.-M Ho, "Aqueous foam flow in microfluidic devices" to be submitted to *Phys. of Fluids*.
23. M. Tatineni and X. Zhong, "Numerical Study of 2-Phase Flows in Microchannels Using the Level Set Method, presented at and part of the proceedings of the 42nd AIAA Aerospace Sciences Meeting and Exhibit, Reno, Nevada, 2004 Paper No.: AIAA-2004-092.
24. M. Tatineni and X. Zhong, "Numerical Simulations of Two-Phase Flows in Micro Gas/Liquid Mixing Sections", AIAA Paper No.:AIAA-2005-1392.
25. T. Cubaud, U. Ulmanella, and C.-M. Ho, "Multiphase flow in microchannels with surface modifications" 5th International Conference on Multiphase Flow, Yokohama, Japan, May 30-June 4, 2004.
26. U. Ulmanella, T. Cubaud, P. K. Wong, T-H. Wang, Y-K Lee, C. Shih, C-M. Ho, "Visualizing heterogeneous flows in micro fluidic devices",



Keynote Speech, The 7th Asian Symposium on Visualization, Singapore,
Nov 2003.

**Laila Abdalla**

Fund Manager

TEL.: (310)206-6999

FAX: (310)206-4830

e-mail: abdalla@ea.ucla.edu<http://fundmgmt.mae.ucla.edu/>

MECHANICAL AND AEROSPACE ENGINEERING DEPARTMENT

48-121 ENGINEERING IV, BOX 951597

Los Angeles, CA 90095-1597

8 July 2005

Ms. Barbara Robertson
ATTN: AMSAM-RD-WS-DP-TD
U.S. Army Aviation and Missile Command
Bldg. 7804, Room 211
Redstone Arsenal, AL 35898-5248

RE: Contract/Grant No. DAAH01-1-R001

Dear Ms. Robertson:

On behalf of Professor Xiaolin Zhong, Principal Investigator, the final technical report for the above-referenced grant is attached. In addition, a pdf copy has been transmitted to you via e-mail.

Please feel free to contact me if I can be of further assistance.

Sincerely,

A handwritten signature in cursive script that reads "Laila Abdalla".

Laila Abdalla

Sponsored Research Fund Manager

Encl: as stated

cc: X. Zhong, UCLA MAE
C.-M. Ho, UCLA MAE
C.-J. Kim, UCLA MAE
X. Zhang, Berkeley ME
C. Gilbert, UCLA OCGA
MAE file
W. Tang, DARPA
V. Lefevre, U.S. Army Aviation
T. Hudson, U.S. Army Aviation
AMSAM-RD-OB-R
OASB/DARPA Library
Defense Technical Information Center

:cg